

2014

Analysis of microseismic events associated with hydraulic fracture propagation

Chennu Fan

Louisiana State University and Agricultural and Mechanical College

Follow this and additional works at: https://digitalcommons.lsu.edu/gradschool_theses



Part of the [Petroleum Engineering Commons](#)

Recommended Citation

Fan, Chennu, "Analysis of microseismic events associated with hydraulic fracture propagation" (2014).
LSU Master's Theses. 3281.

https://digitalcommons.lsu.edu/gradschool_theses/3281

This Thesis is brought to you for free and open access by the Graduate School at LSU Digital Commons. It has been accepted for inclusion in LSU Master's Theses by an authorized graduate school editor of LSU Digital Commons. For more information, please contact gradetd@lsu.edu.

ANALYSIS OF MICROSEISMIC EVENTS ASSOCIATED
WITH HYDRAULIC FRACTURE PROPAGATION

A Thesis

Submitted to the Graduate Faculty of the
Louisiana State University and
Agricultural and Mechanical College
in partial fulfillment of the
requirements for the degree of
Master of Science

in

The Department of Petroleum Engineering

by

Chennu Fan

B.S., University of Science and Technology of China, 2010

May 2014

Acknowledgments

I am grateful to my advisor, Dr. Arash Dahi Taleghani, for providing me with the opportunity to carry out microseismic and hydraulic fracturing research in petroleum engineering in Louisiana State University. I sincerely appreciate his instructions and help in assisting me to finish my thesis. I also thank Dr. Juan Lorenzo, my co-advisor, for the vivid explanations of geophysics puzzles and help in writing my thesis. I want to thank them for the doors they has opened and the passion they has instilled. I greatly benefit from their detailed guidance and scientific insight throughout my Master study. I would also like to acknowledge my committee: Dr. Smith and Dr. Sears for their advice and help on my thesis.

I wish to express my gratitude to Schlumberger Unconventional Resources and Louisiana Board of Regents for supporting this research.

I would also like to thank Craft and Hawkins Department of Petroleum Engineering at LSU.

I also wish to thank all my group members: Wei Wang, Houman Bedayat, Miguel Gonzalez-Chavez, Milad Ahmadi, Denis Klimenko, and Ping Puyang for their help in this research.

My final and most heartfelt acknowledgement must go to my parents. I greatly thank them for the endless love and supporting and caring for me all of my life.

Table of Contents

Acknowledgments	ii
Abstract	v
Chapter 1: Introduction	1
1.1 Hydraulic Fracturing	1
1.2 Assessment of Hydraulic Fracturing Treatment	6
1.3 Research Goal	9
1.4 Research Objectives	9
1.5 Justification	10
Chapter 2: Theoretical Microseismic Seismograms	12
2.1 Introduction	12
2.1.1 Seismic waves from a point dislocation source	12
2.1.2 Double couple source	15
2.2 Seismic Waves in a Homogenous and Isotropic Medium	16
2.2.1 Seismic waves from a point dislocation source	16
2.2.2 Double couple and compensated linear vector dipole source .	20
2.2.3 Intermediate-field and near-field effects	31
2.2.4 Noise effects	32
2.3 Seismic Waves in a Homogeneous and Anisotropic Medium	34
2.3.1 Double couple and compensated linear vector dipole source with vertically symmetric anisotropy	37
2.3.2 Noise effects	39
2.4 Conclusions	39
Chapter 3: Source Mechanisms during Hydraulic Fracturing	43
3.1 Introduction	43
3.2 A Source Mechanism Study for a Homogeneous and Isotropic Medium	45
3.2.1 Moment tensor inversion for synthetic seismograms	46
3.2.2 Moment tensor inversion for synthetic seismogram with noise	51
3.3 A Source Mechanism Study for a Homogeneous and Anisotropic Medium	54
3.4 Conclusions	58
Chapter 4: Summary, Conclusions and Recommendations	60

4.1	Summary of Research	60
4.2	Conclusions	61
4.3	Recommendations	62
	References	64
	Appendix A: Synthetic Seismogram Calculation	72
	Appendix B: Moment Tensor Retrieval - A MATLAB GUI	93
	Appendix C: Steps for Inversion by ISOLA	97
	Vita	100

Abstract

Previous practice to determine the source mechanism of microseismic events associated with hydraulic fracture typically includes only far-field terms in moment tensor inversion. The intermediate-field terms and near-field term are normally ignored because of increased complexity in the calculation. Source-receiver distances in hydraulic fracturing are usually 1000 ft and the effects of near and intermediate-field terms are still unknown. We perform a study to improve the precision of the source mechanism by including the intermediate-field term in moment tensor inversion.

We find that the intermediate-field term contributes $1/3$ of the signal amplitude when the source-receiver distance is 1000 ft. The intermediate-field term contributes $1/20$ of the signal amplitude when the source-receiver distance is 6700 ft. Note that " $1/20$ " is at the noise level. Thus, when source-receiver distance is less than 6700ft, we need to consider the intermediate-field term. Especially, when the distance is 1000ft, the intermediate-field term becomes significant. Similarly, near-field terms contribute less than $1/20$ of the signal amplitude when distances are larger than 300 ft. In our case, we confirm that the near-field term can be ignored in microseismic analysis.

Our results indicate that the intermediate-field terms can improve moment tensor inversion by 2% to 40% at source-receiver ranges less than 1000 ft. When distances are larger than 6700, the improvement is limited to 1%. In the presence of noise, the intermediate-field terms help to improve the moment tensor inversion (15% improvement with noise present vs 3% improvement without noise). Our study provides a foundation for using intermediate-field terms in moment tensor inversion in the studies of hydraulic fractures.

Chapter 1

Introduction

1.1 Hydraulic Fracturing

Microseismic mapping is a passive seismic approach that has been used for assessment of hydraulic fracture treatments during the last two decades. By mapping microseismic events and determining their source mechanism, the location, geometry, length, width, and the height of hydraulic fracture can be estimated. Dimensions and geometry of induced fractures can be used to improve the design of future fracturing treatments and building better reservoir simulations to predict well performance in the future. This chapter gives a brief introduction about hydraulic fracturing treatments and microseismic technology, as well as limitations of this technology. Possible ways are proposed to improve the reliability in interpreting microseismic data collected in the field.

Hydraulic fracturing was first used by the oil and gas industry during the 1930s when the Dow Chemical Company discovered that by applying a sufficiently large fluid pressure, it is possible to fracture the rocks around the borehole to improve the effectiveness of acid stimulation treatments (Grebe et al. 1935). The first non-acid hydraulic fracturing treatment for wellbore stimulation was performed in Kansas in 1947 in a gas well in Hugoton field (Veatch et al. 1989). Today, hydraulic fracturing is widely used to improve oil and gas productivity. About 70% of gas wells and 50% of oil wells have been fractured hydraulically in North America since the 1950s (Valko and Economides, 1995). Thousands of treatments are implemented each year in different geological formations, for example, in jointed granite (House, 1987) to improve the efficiency of a geothermal reservoir (Drader et al., 2012), in

tight gas sandstones (Northrop and Frohne, 1990), low permeability sandstones (Martins et al., 1992) and shale (Rosen, 1994).

Hydraulic fracturing induces fractures in rock in the subsurface and thereby increases the overall permeability of the formation and facilitates the flow of petroleum, water, and natural gas as a result. In general, this method may be used from shallow to deep formations (Figure 1.1). Where there is a risk of developing hydraulic fractures into the shallow aquifer, monitoring fracture size during treatment and its post-treatment estimation can be important to guarantee water quality (Willson et al., 1993). Warpinski (1991) reports that natural gas production in low permeability sand reservoirs in Piceance basin and Greater Green River basin increased from an average initial production rate of 250 Mscf/day to 450 ~ 500 Mscf/day after the treatment. Miller et al. (2008) points out that long-term production in Bakken Shale Formation in North Dakota of the Williston Basin has improved 91% after hydraulic fracturing stimulations. A tight gas reservoir in Saudi Arabia initially produced 8 million standard cubic feet per year and then proceed to 240 million cubic feet per year after hydraulic fracturing (Rabim et al., 2012).

Hydraulic fracturing can be one of the most complicated procedures performed on a well. This is partially due to the high flow rates and pressures, large volume of materials injected, continuous blending of materials and large amount of unknown variables (Economides and Nolte, 2008). If the fluid is pumped into a well at a rate faster than it escapes into the formation, pressure can rise and even break rock at some points (Economides and Nolte, 2008). High pressure fluid can break the formation and result in the wellbore splitting along its axis as a result of tensile hoop stresses (Economides and Nolte, 2008). In general, hydraulic fractures are

created as a consequence of the action of the large fluid pressure (Economides and Nolte, 2008).

During injection the fluid starts leaking into the formation until hydraulic fractures initiate. If the pumping rate is maintained at a rate that is higher than the fluid-loss rate, the newly created fractures will continue to grow (Economides and Nolte, 2008). More of the rock formation is exposed concomitant with the growth of hydraulic fractures. Once pumping stops and the injected fluids leak off, the fracture will close under the ambient pressure and the created contact area inside the rock will no longer be available to enhance fluid production. To prevent fracture closure, measures must be taken to keep the conductive channels open (Economides and Nolte, 2008). This normally involves adding a propping agent to the fluid to be pumped into the fracture. When pumping stops and fluid flows back to the well, the propping agent remains in place to keep the fracture open and it maintains a conductive flow path for the increased formation flow area during production. The propping agent is generally sand or a high strength, granular substitute for sand (Economides and Nolte, 2008).

Initially, fracture penetration is limited, and hence fluid loss is high near the wellbore. For this reason, the first part of a hydraulic fracture treatment uses gel fluid mainly. This period of fluid injection is named 'pad stage' (Economides and Nolte, 2008). After this stage, propping agent with fluid is pumped into the fracture. As the fluid loss to the formation decreases, the proppant is added to the fluid at lower concentrations. With fluid loss, proppant concentration increases. The final phase of the treatment is called the 'flush stage'. This stage is intended to sweep the wellbore clean of gels and leaves an almost clean proppant-filled fracture (Economides and Nolte, 2008).

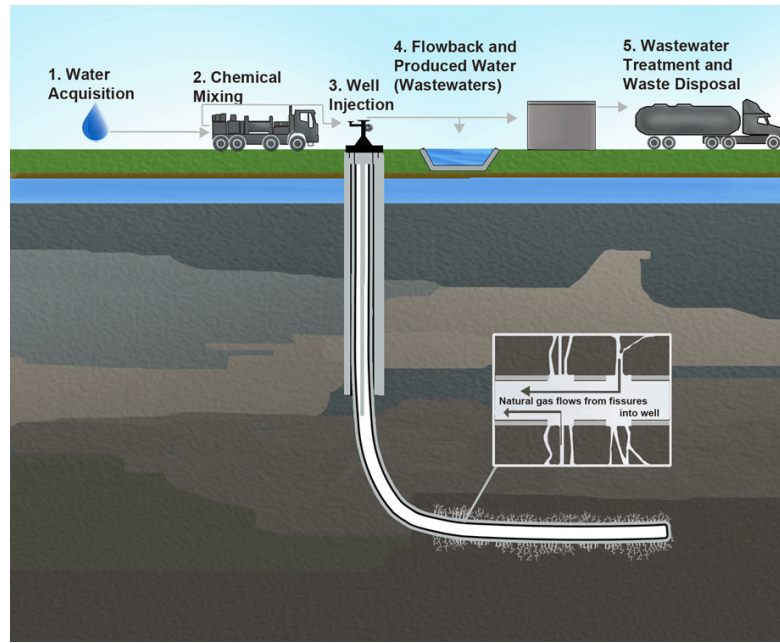


FIGURE 1.1. The numbers list the procedure during hydraulic fracturing. First, water is acquired (1) and then mixed with proppant or chemical additives (2). Next, the fluid is injected into the treatment well and the fractures are generated in the formation (3). The waste water flow back (4) and is treated (5) before disposal (Environmental Protection Agency, 2012).

Multi-stage hydraulic fracturing stimulation treatments are utilized in many reservoirs with low effective permeability, low pressure, high water production, to increase the productivity of wells, especially in gas reservoirs that cannot produce adequately without stimulation. Multi-stage fracturing is normally used in long horizontal wells (McDaniel et al., 2006). In horizontal wells, the producing portion of the well is usually the cased horizontal section of the wellbore that lies entirely in the producing formation. It is the portion of casing which would be perforated with perforating guns for hydraulic fracturing purposes and future gas production. To communicate with the target outside formation that contains the natural gas, the horizontal section of the casing must be perforated. This is done at various intervals in the complete horizontal section along the reservoir. The intervals along the horizontal portion of the casing are usually perforated in stages. This job is carried out mainly in two ways: 'Plug and Perf' or sliding sleeve. 'Plug and

Perf' is the process whereby the horizontal casing in the horizontal wellbore is perforated, and then plugged at intervals starting from the end of the wellbore in the backward direction. 'Plug and Perf' repeated in several intervals is named multi-stage hydraulic fracturing.

A schematic picture of multi-stage hydraulic fracturing is shown in figure 1.2. Six fracturing stages are executed in each horizontal well. The distance interval between each stage depends on the pay zone thickness that the treatment is designed for (Zimmer et al., 2009). In the shown example, the distance between stages is 250 m. In the drained zone (or stimulated zone), the overall permeability is enhanced around each set of perforations.

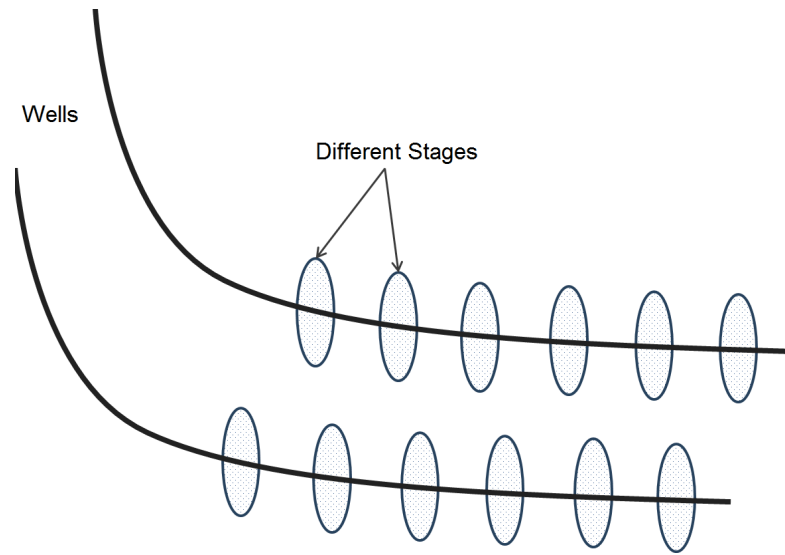


FIGURE 1.2. Multiple hydraulic fracture stages along the well axis for shale gas stimulation.

Hydraulic fracturing is also used in enhancing geothermal energy extraction (Sasaki, 1998; Berumen et al., 2000), for hazardous solid waste disposal (Hunt et al., 1994; Hailey et al. 1999), measurement of in-situ stresses (Hayashi et al., 1997; Raaen et al., 2001), fault reactivation in mining (Board et al. 1992) and remediation of soil and ground water aquifers (Murdoch and Slack 2002). Hydraulic fractures

may induce seismicity by deforming the formation, so they can also be imaged by somehow acquiring microseismic emitted waves, which mainly relies on the detection and quality of microseisms or acoustic emissions associated with fracture propagation (House, 1987; Urbancic et al., 1999; Maxwell et al., 2002).

1.2 Assessment of Hydraulic Fracturing Treatment

Three groups of technologies have been used in the oil and gas industry to provide an overall picture of induced hydraulic fracturing: Far field direct group, near-wellbore direct group, and indirect group. In the far-field direct group, there are two common methods to analyze the fracture: tiltmeter analysis (Wright, 1998) and microseismic analysis (Warpinski et al., 1998). Tiltmeter Analysis provides the fracture orientation and geometry by measuring the tilt in the downhole or ground surface. The main limitation of the tiltmeter approach is its strong dependency on the location of the instrument and the distance between tiltmeters and induced fractures. In the case of development of complex fracture networks, application of tiltmeters is very limited because of inadequate measurement points (Wright, 1998). On the other hand, microseismic analysis provides an image of the fracture by detecting microseismic waves emitted from fracture front.

In the near-wellbore direct measurement group, Caliper logging (Potter, 1977), production logging (PLT) (Paillet, 1998), and borehole image logging (Williams and Johnson, 2004) are examples of near-wellbore methods. The major limitation of these techniques is that an open hole is needed to run most of the tools and they mainly provide information about fracture height at the wellbore, not fracture length or its geometry. In the indirect group, production analysis, well testing, net pressure fracture analysis, or any combination of these methods are used to map hydraulic fractures (Wright, 1998). The results of these methods strongly depend on model assumptions about formation properties or natural fracture distribution

as the bottomhole pressure and the production rate does not provide enough data to solve the inverse problem of determining fracture geometry. The overall picture of hydraulic fracturing generated by these methods will not be unique (Wright, 1998).

Nowadays, industry is more interested in using microseismic analysis to assess hydraulic fracturing jobs as it is more tangible and less dependent on the location of the instrument in comparison to tiltmeters. This technology has been studied since 1968 (Knill et al., 1968) that shows that rockbursts or fractures induce seismic events. The magnitude of these events is reported to be between $M -2.0$ to 2.5 . Fracture tips are usually considered as the location of seismic source. These low magnitude induced events are termed microseismic events. Microseismic analysis may be used to provide a rough image of the fractures by connecting the detected locations of microseismic events mainly triggered by shear slippage on bedding planes or natural fractures intersected by the hydraulic fracture (Warpinski et al., 1998).

During microseismic monitoring of hydraulic fracturing treatments, seismic sensors need to be placed in appropriate positions. From the data they collect, small earthquakes induced during cracking of the rock can be detected and located within the formation. Arrays of sensitive receivers are placed typically in an offset well at a depth relatively close to the treatment well (500 ft to 3000 ft) or in the absence of any nearby well, these sensors are placed on the ground surface. The arrays of detectors collect seismic waves generated by propagating fractures. Detectors can be three-component geophones or accelerometers (Hon et al., 2008). Geophones and accelerometers are simple harmonic oscillators that consist of a proof mass suspended from damped springs. The motion of the proof mass with reference to the ground and sensor case is recorded as signal (Hon et al., 2008). Different geo-

phones and accelerometers are sensitive for a band of frequencies depending on the design. Accelerometers are sensitive for low frequency waves, below 5 Hz. On the contrary, geophones are sensitive in a band of 5 to 200 Hz (Hon et al., 2008). The frequency range of the microseismic data that can be used for practical purposes is between 10 Hz and less than 1000 Hz (Hon et al., 2008). Comparing the frequencies ranges of microseismic data between geophone and accelerometers, geophones are more sensitive for microseismic data. Therefore, geophones are usually used to record microseismic events.

The acquired data are processed in several steps to locate events using an assortment/collection of information obtained from compressional (P-wave) and shear (S-wave) arrivals detected by the array (Warpinski, 2009).

A part of the microseismic waves detected in the field are generated by induced shear slippage in the formation either along natural fractures or natural fractures intersected by the hydraulic fracture (Cipolla and Wright, 2000). With proper fracture diagnostic measurements, the length, height, asymmetry, width, azimuth, dip and volume of the fractures can be detected. As a result, a reservoir can be understood and managed. Microseismic fracture mapping suffers several limitations including instrument sensitivity and noise in the well field (Warpinski et al., 2008). The location error can be 52 ft (16 m) when the source-receiver distance is 1000 ft (305 m) (House, 1987), and the error increases to 350 m (1148 ft) in location when the source-receiver distance is 900 m (2953 ft) (Zimmer, 2010).

The elastodynamics of the microseismic events can be calculated from microseismic data and it is termed source mechanism. The applied force can be calculated from source mechanism. The term source mechanism or focal mechanism conventionally refers to fault orientation, the displacement and stress release patterns and the dynamic process of seismic wave generation. Source mechanism is traditionally

determined using first-motion data to constrain a single, double-couple mechanism. The source mechanism can be replaced by moment tensor solutions. The moment tensor can be decomposed in terms of its principal axes, and the eigen values as well as the directions of the eigen vectors. From a good source mechanism, we can know the failure mechanism that creates the reservoir stimulation. From the first motion of P waves and S waves, we can obtain the principle orientation of the slippage plane, the direction of dip, strike and rake of the fracture. Using these angles, the source mechanism and moment tensor can be quantified as well as the percent of shear crack and volumetric components.

1.3 Research Goal

Considering that microseismic technology is mainly limited by the low resolution of field data and a noisy environment, the research goal of this thesis is set to improve the accuracy of the source mechanism in processing hydraulic fracturing data. More accurate information about the source mechanism will help us to have a better understanding of complexity of failure mechanisms.

1.4 Research Objectives

The objectives of the research are as follows

1. Calculate seismic waveforms generated by an artificial source as a function of distance and position of the receivers with respect to the source. The source is assumed to be a static double-couple or compensated linear vector dipole; and the medium is assumed to be elastic, isotropic and homogeneous. A MATLAB program is developed to obtain the seismic waveforms. Far-field, intermediate-field, and near-field components of waveforms are produced.
2. Calculate seismic waveforms as a function of distance and position with respect to different source-receiver distances. The source is a static moment tensor; and the medium is assumed to be anisotropic and homogeneous. A MATLAB program

is developed to obtain the seismic waveforms. Far-field, intermediate-field, and near-field components of waveforms are produced.

3. Locate micro-tremors and obtain the associated moment tensor using an open source MATLAB program called ISOLA (Sohos and Zahradnik, 2008). First P and S wave arrival time will be used to locate the source. To examine the accuracy and efficiency of the applied inversion technique to retrieve moment tensors. I will invert the synthetic seismograms produced in objectives 1 and 2 for whom the source mechanism is known.

4. Compare seismograms forward modeled with far-field, intermediate-field, and near-field. Use the inversion technology developed stage 3 to obtain the moment tensor inversion to compare the difference among moment tensor inversion of the seismograms with only far-field terms and far- and intermediate-field terms. Explain the difference in focal mechanism among different seismograms. The results will show the potential role of intermediate-field terms in changing the interpretation from fracture patterns at various source-receiver distances.

1.5 Justification

The current approach in the industry for microseismic analysis is based on the knowledge developed over decades on analyzing earthquakes, but microseismic source in hydraulic fracturing jobs are much closer to the receivers than earthquakes are to seismograph stations in general. Therefore, we need to evaluate this fact in locating events and moment tensor inversion of these events. Aki and Richards (2002) point out that the far-field terms in the displacement solution for double-couples are suitable for situations where the receivers are located more than a few wavelengths away from the source, and that the near- and intermediate-field terms are meaningful for positions within a small fraction of a wavelength from the source. At near and intermediate distances, the magnitude of each term should

be assessed. Ichinose et al. (2000) point out that at some certain frequencies and distances, the near- and intermediate-field terms are important for waveform modeling and moment tensor inversion. The significance of including intermediate- and near-field terms has also been highlighted by Lokmer and Bean (2010) in the study of long-period wavefields produced by volcanoes. The errors in source location decrease when the near- and intermediate-field terms are considered.

Chapter 2

Theoretical Microseismic Seismograms

2.1 Introduction

Generation and emission of microseismic waves is a complex problem as it occurs in the rock layers which are not homogeneous and isotropic. However, to understand the physics behind this phenomenon, it is easiest to start with a simple model.

The hydraulic fracture can be assumed to behave as a seismic source, which generates body waves, P-waves, and S-waves. Two types of sources can be considered: a single point dislocation source and a moment tensor source (Aki and Richards, 2002).

The single point dislocation is the simplest approximation for seismic sources. The source has small dimensions compared to the wavelengths. However, the real source may be a composite source, which is both temporally and spatially variable. The moment tensor is a useful approximation to general sources including faults and tensile fractures. The spatial analysis of seismic sources is usually performed by using a moment tensor (Aki and Richards, 2002). A double-couple source is a special moment tensor used to describe the equivalent body forces for a shearing fault.

2.1.1 Seismic waves from a point dislocation source

In a single point dislocation source, the source is treated as a mathematical point with no size, shape or mass and represents the simplest analytical case for studying seismic problems (Backus and Mulcahy, 1976). In this case, the medium is assumed to be infinite, homogenous, isotropic, and linear elastic (Mavko et al. 1998). No reflection or refraction waves are generated under these assumptions since the

considered medium does not have a boundary; thus, the geophones only receive direct waves.

The source is a displacement. The wave is the earth's response immediately after the initial displacement ($\vec{u}(\vec{x}, t)$). For a single point body-force \vec{f} , the displacement $\vec{u}(\vec{x}, t)$ is given by Aki and Richards (1980).

$$\rho \ddot{\vec{u}} = \vec{f} + (\lambda + 2\mu) \nabla(\nabla \cdot \vec{u}) - \mu \nabla \times (\nabla \times \vec{u}). \quad (2.1)$$

(Eq. 4.1 Aki and Richards, 1980)

where ρ is the density of the rock, and λ and μ are *Lamé's* parameters, which describe the relationship between stress and strain.

At $t < 0$, before the seismic wave is generated, the displacement and the velocity ($\dot{\vec{u}}$) are zero:

$$\vec{u}(\vec{x}, 0) = \vec{0} \quad (2.2)$$

and

$$\dot{\vec{u}}(\vec{x}, 0) = \vec{0} \quad (2.3)$$

for $\vec{x} \neq \vec{0}$.

Helmholtz decomposition is used to separate displacement caused by the P-wave and S-wave, since displacements caused by a P-wave are curl-free but those by S-wave are inherently divergence-free. Any vector on a bounded domain, which is twice continuously differentiable, can be decomposed into a curl-free component and a divergence-free component (Aki and Richards, 2002).

The body force and initial values of \vec{u} and $\dot{\vec{u}}$ can also be expressed in terms of Helmholtz potentials so that

$$\vec{f} = \nabla \Phi + \nabla \times \vec{\Psi} \quad (2.4)$$

At the same time, there exist potentials ϕ and $\vec{\psi}$ for \vec{u} with the following four properties:

$$\vec{u} = \nabla\phi + \nabla \times \vec{\psi}, \quad (2.5)$$

$$\nabla \cdot \vec{\psi} = 0, \quad (2.6)$$

$$\ddot{\phi} = \frac{\Phi}{\rho} + \alpha^2 \nabla^2 \phi \quad (\text{with } \alpha^2 = \frac{\lambda + 2\mu}{\rho}), \quad (2.7)$$

$$\ddot{\vec{\psi}} = \frac{\vec{\Psi}}{\rho} + \beta^2 \nabla^2 \vec{\psi} \quad (\text{with } \beta^2 = \frac{\mu}{\rho}) \quad (2.8)$$

$\nabla\phi$ and $\nabla \times \vec{\psi}$ are called the P-wave and S-wave components, respectively, and $\nabla \times \vec{\Phi}$, $\nabla \cdot \vec{\Psi}$ are equal to 0.

Using equations 2.5 through 2.8, the displacements are calculated as:

$$\begin{aligned} u_i(\vec{x}, t) = & \frac{1}{4\pi\rho} \left(3 \frac{x_i}{r} \frac{x_j}{r} - \delta_{ij} \right) \frac{1}{r^3} \int_{r/\alpha}^{r/\beta} \tau X_0(t - \tau) d\tau \\ & + \frac{1}{4\pi\rho\alpha^2} \frac{x_i}{r} \frac{x_j}{r} \frac{1}{r} X_0\left(t - \frac{r}{\alpha}\right) \\ & - \frac{1}{4\pi\rho\beta^2} \left(\frac{x_i}{r} \frac{x_j}{r} - \delta_{ij} \right) \frac{1}{r} X_0\left(t - \frac{r}{\beta}\right) \end{aligned} \quad (2.9)$$

(Eq. 4.23 Aki and Richards, 1980)

where α and β are compressional and shear wave velocities related to *Lamé's* constants and which can also be obtained from the Young's modulus and Poisson's ratio. In equation 2.9, \vec{x} is the location vector of each geophone, r is the distance from source to geophone, and t is time. The seismic wave is presented by an impulse combined with harmonic sine functions: $X_t = [0, \sin(b \cdot t), 0]$. $X_0(t)$ is the impulse in the x_j -direction at the origin. δ_{ij} is a Kronecker delta, and τ represents the time that a unit impulse is applied with the condition $\tau < t$.

2.1.2 Double couple source

A shear source mechanism can be represented as a double couple dislocation (the definition of double couple and moment tensor can be found in Chapter 3). In the case of a double couple, angular momentum is not conserved unless a complementary couple exists to balance the present couple. The resulting pair of couples is termed as a double couple (Bullen and Bolt, 1985; Nettles and Ekstrom, 1998). In general, a double couple can be used to represent movement along either of two conjugate fault planes.

The displacements caused by a double couple can be calculated by superposing the solutions of far-field, intermediate-field, and near-field term displacements (Aki and Richards, 2002). The equations below describe the displacements that are caused not only by a double-couple source, but also by any moment tensor source (Aki and Richards, 2002; Madariaga, 2007). The following equation shows all the terms of displacements.

$$\begin{aligned}
u(\vec{x}, t) = & \frac{1}{4\pi\rho} \vec{A}^N \frac{1}{r^4} \int_{r/\alpha}^{r/\beta} \tau M_0(t - \tau) d\tau \\
& + \frac{1}{4\pi\rho\alpha^2} \vec{A}^{IP} \frac{1}{r^2} M_0(t - \frac{r}{\alpha}) + \frac{1}{4\pi\rho\beta^2} \vec{A}^{IS} \frac{1}{r^2} M_0(t - \frac{r}{\beta}) \\
& + \frac{1}{4\pi\rho\alpha^3} \vec{A}^{FP} \frac{1}{r} \dot{M}_0(t - \frac{r}{\alpha}) + \frac{1}{4\pi\rho\beta^3} \vec{A}^{FS} \frac{1}{r} \dot{M}_0(t - \frac{r}{\beta})
\end{aligned} \tag{2.10}$$

(Eq. 4.32 Aki and Richards, 1980)

where we used the same definitions for the symbols as in the expression for a single point dislocation source. M_0 is the seismic moment. The definition of r , θ , and ϕ in radiation patterns is shown in Figure 2.1. The near-field radiation pattern is represented as:

$$\vec{A}^N = 9\sin 2\theta \cos \phi \hat{r} - 6(\cos 2\theta \cos \phi \hat{\theta} - \cos \theta \sin \phi \hat{\phi}) \tag{2.11}$$

\vec{A}^{IP} and \vec{A}^{IS} represent intermediate-field radiation pattern:

$$\vec{A}^{IP} = 4\sin 2\theta \cos \phi \hat{r} - 2(\cos 2\theta \cos \phi \hat{\theta} - \cos \theta \sin \phi \hat{\phi}) \quad (2.12)$$

$$\vec{A}^{IS} = -3\sin 2\theta \cos \phi \hat{r} + 3(\cos 2\theta \cos \phi \hat{\theta} - \cos \theta \sin \phi \hat{\phi}) \quad (2.13)$$

\vec{A}^{FP} and \vec{A}^{FS} represent far-field radiation pattern:

$$\vec{A}^{FP} = \sin 2\theta \cos \phi \hat{r} \quad (2.14)$$

$$\vec{A}^{FS} = \cos 2\theta \cos \phi \hat{\theta} - \cos \theta \sin \phi \hat{\phi} \quad (2.15)$$

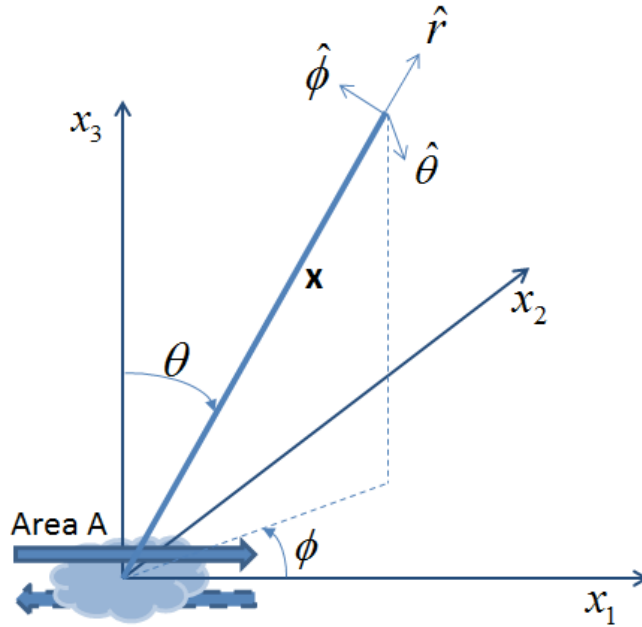


FIGURE 2.1. The definition of r , θ , and ϕ in radiation patterns.

2.2 Seismic Waves in a Homogenous and Isotropic Medium

2.2.1 Seismic waves from a point dislocation source

A common porous reservoir rock that can accumulate oil and gas is typically sandstone or shale. Because of its extremely low permeability, shale reservoirs are considered unconventional. To model the seismogram from a single point source, we

use the parameters in Table 2.2. Comparing the parameters in Table 2.2 with Table 2.1, one can easily find out that the parameters can be represented both sandstone or shale.

TABLE 2.1. The rock parameters for sandstone and shale (Mavko, 1998)

	Sandstone	Shale
Density (g/cm^3)	2.09 - 2.67	2.00 - 2.40
Young's Modulus (GPa)	3.24 - 99.9	4.00 - 18.0
Poisson's ratio	0.2 - 0.35	0.2 - 0.35
P wave velocity (km/s)	3.13 - 5.52	1.10 - 2.50
S wave velocity (km/s)	1.73 - 3.60	0.2 - 0.8

TABLE 2.2. The rock parameters used in generating synthetic seismograms shown in this thesis

Density (g/cm^3)	2.30
Young's Modulus (GPa)	10.0
Poisson's ratio	0.3

In order to calculate synthetic seismograms as may be collected in a vertical borehole, we distribute theoretical receivers vertically and place an arbitrary source at the origin (0, 0, 0). The force at the source is 0.1 N, see Figure 2.2. The dominant frequency of the seismic wave is picked as 100 Hz, since the frequency range from the real microseismic events associated with hydraulic fracture is from 10 to 1000 Hz. The tenth receiver is the middle one, and locates at (0, 100, 0). We also set the direction of the pure P-wave propagate as positive. Because the whole seismograms are complex to study and each component is linear, we separate the whole seismograms into the seismograms contain only P-wave components, and ones with only S-wave components.

In the resultant calculation of synthetic seismograms, receivers at different locations record the expected behavior from the source. The displacement caused by S-wave versus time in x-direction is always zero for each receiver (Figure 2.3 x-direction). This is consistent with our expectation since the original source

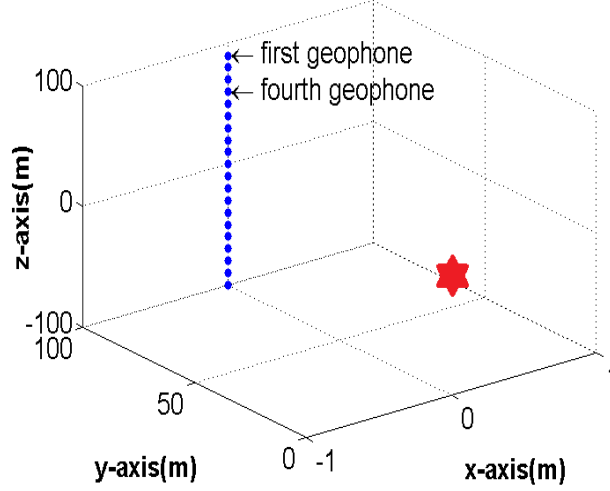


FIGURE 2.2. Arrangement 1: Source-receiver geometry used for calculation. A dot represents a geophone. The single dislocation source is at (0,0,0). The dots represent a set of vertical receivers within the depth of -100 to 90 meters. They are placed at 100 meters distance from the source in y-direction. The results are shown in the Figure 2.2 and 2.3. Note that the geophones are equally spaced and the first one is located at $z = 100$ m.

$X_t = [0, \sin(100 \cdot t), 0]$ only have a non-zero amplitude in y-direction, while all the receivers are in the line of $x = 0$. The displacement caused by S-wave versus time in y-direction is zero only when $x = z = 0$ at geophone No. 10, that matches the definition of S-wave (Figure 2.3 y-direction). At longer source-receiver distances away from $z = 0$, the S-wave amplitudes are larger (Figure 2.3 y-direction). the middle line is represented $z = 0$, the lines next to it have the same x and y, $z = \pm 10$, and we can clearly find out that the displacement increases step by step (Figure 2.3 y-direction).

The velocity is the derivative of the displacement respect to time. When the displacement increases, the velocity is positive; when the displacement decreases, the velocity is negative; when no change with displacement, the velocity is zero.

The velocity is constant zero in x-direction, due to the displacement does not change in x-direction (Figure 2.3). the displacement caused by S-wave in z-direction is negative when $z < 0$; and positive when $z > 0$. In our expectation, the displace-

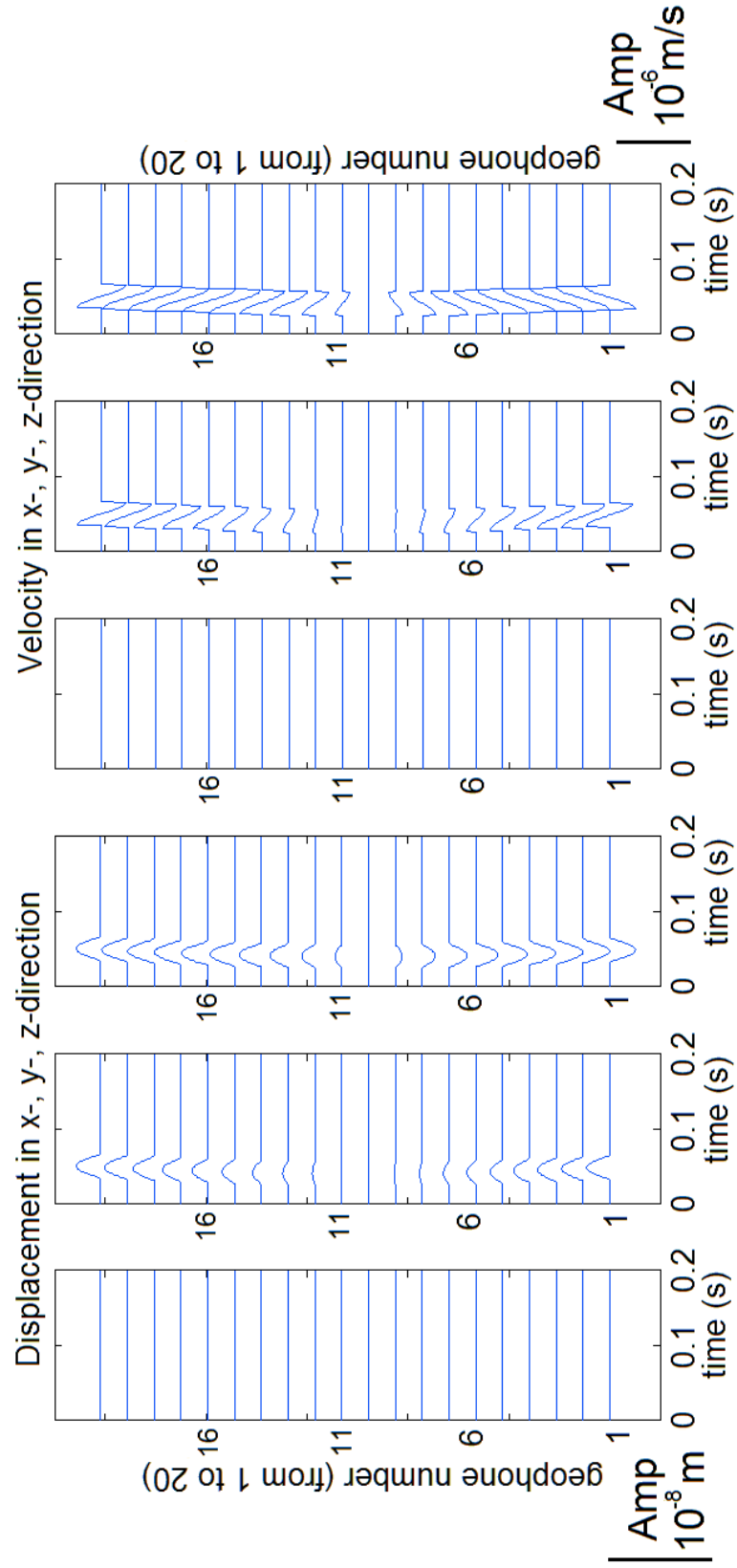


FIGURE 2.3. Geophones: displacement and velocity induced by S-wave in x-, y-, z-direction vs. time.

ment is zero when $x = z = 0$. The S-wave has a non-zero displacement when x or z is not equal to zero. In x or z direction, the displacement is larger than zero in the negative half of the x - or z -axis; because the direction of the pure P-wave propagation direction is positive. Meanwhile, the displacement caused by S-wave has a minus sign in the formula.

Similarly, the displacement in x -direction is zero because the position of all the receivers are at the line of $x = 0$ (Figure 2.4). When P-wave propagates in y -direction, the receiver should get the highest amplitude of P-wave in y -direction and no response for S-wave. The largest amplitude appears at $z = 0$ (Figure 2.4 y -direction). The point of non-zero displacement firstly took place in the line which represents the geophone located at $z = 0$ because the distance between the source and the receiver is the shortest. The displacement is larger than zero when $z > 0$ as also been seen from the Equation 2.10 (Figure 2.4 z -direction).

In field data, we normally receive the composed effect of P and S waves. In synthetic cases, we can simply add the two partial motion (Figure 2.5). Since the displacements caused by P-wave and S-wave are always zero in x -direction, no displacement is in x -direction (Figure 2.5). The displacement has no much difference among all 20 positions (Figure 2.5). The reason is that the displacement caused by P-wave is decreased when the distance increases while S-wave shows an opposite behavior.

The geophones are sensitive to the velocity, thus only velocity information from field in fracturing monitor is record. We will study the velocity information recorded by the geophones.

2.2.2 Double couple and compensated linear vector dipole source

We developed a MATLAB program to simulate the microseismic waves received by geophones. This program aims provides additional intermediate-term and far-

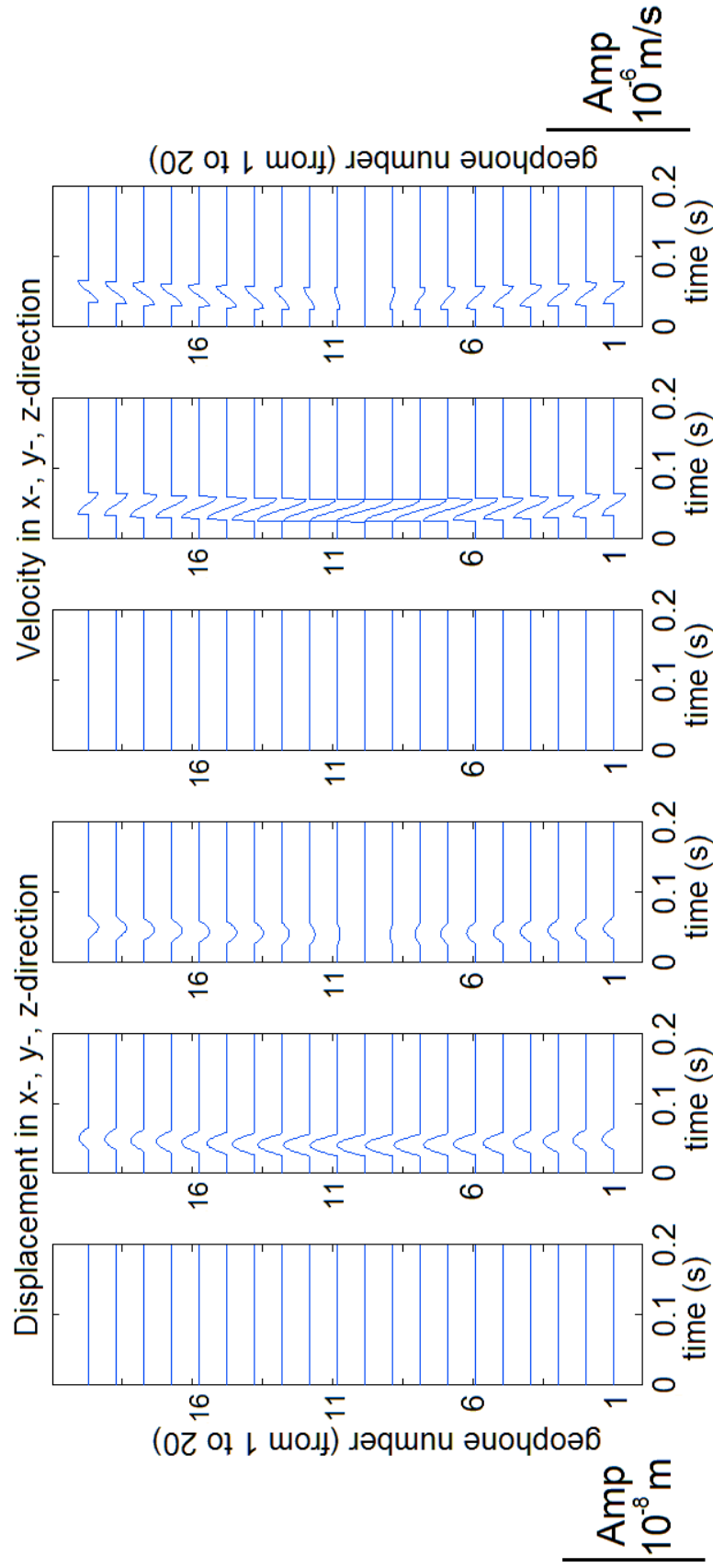


FIGURE 2.4. Geophones: displacement and velocity induced by P-wave in x-, y-, z-direction vs. time.

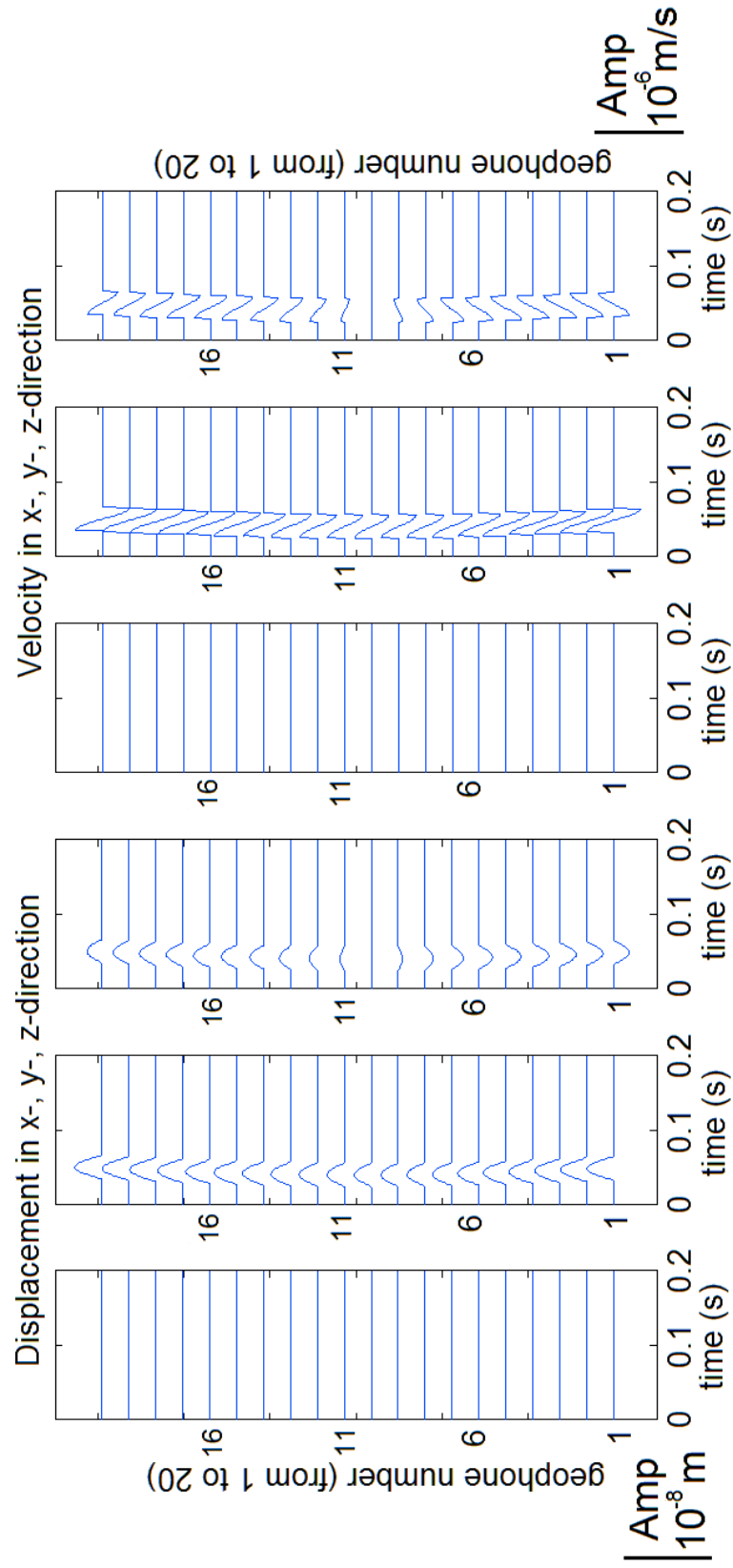


FIGURE 2.5. Geophones: displacement and velocity in x-, y-, z-direction vs. time.

term components in the calculation of the synthetic seismogram and uses a source based on double couple model. The verification of the calculation by this program is accomplished by comparison to the output of a similar MATLAB program: `anaseis.m` (Jahnke, 2004). Anaseis only gives the far-field seismogram caused but does not use a double-couple dislocation source. We adapt similar arrangement from `anaseis.m` (Figure 2.6 and Figure 2.7) to conduct a calculation using both programs. We find that the calculations using my program and anaseis is the same.

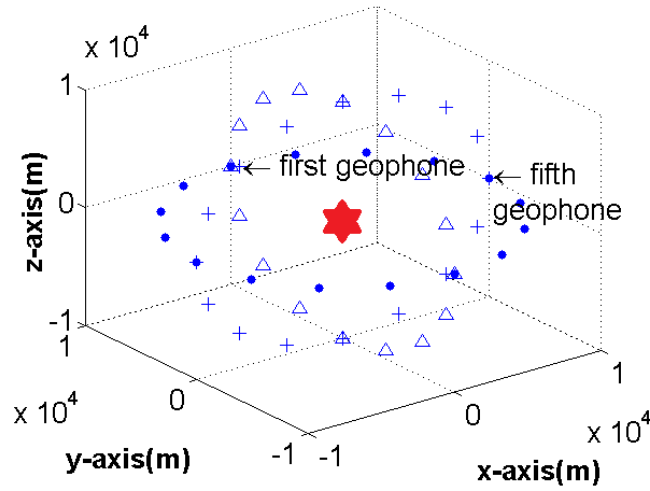


FIGURE 2.6. Arrangement 2: Source-receiver geometry used for calculation. A dot represents a geophone. The double couple source is at (0,0,0). Blue, green and red colors represent the line arrangement parallel to y-, z- and x- axis, respectively.

We also compare our synthetic seismograms radiation pattern diagrams with the prediction by Aki and Richard (1980) using the following moment tensor:

$$M_0 = \begin{bmatrix} 0 & 0 & M_{13} \\ 0 & 0 & 0 \\ M_{31} & 0 & 0 \end{bmatrix}, \text{ which describes the generic moment tensor for a fault surface (Gibbons, 2009) which can be reverse, normal and strike-slip fault surface (Figure 2.8).}$$

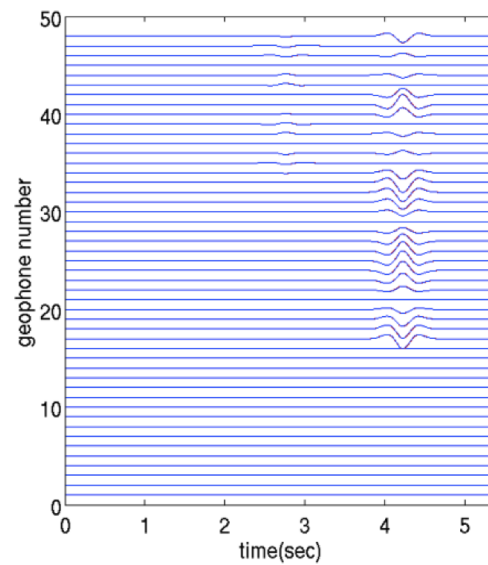


FIGURE 2.7. Comparison of calculated signals from the program we developed and anaseis (G. Jahnke, 2004). The blue line shows the result calculated from our program, and the red line is the result calculated by anaseis.m. The blue lines completely overlap with the red line.

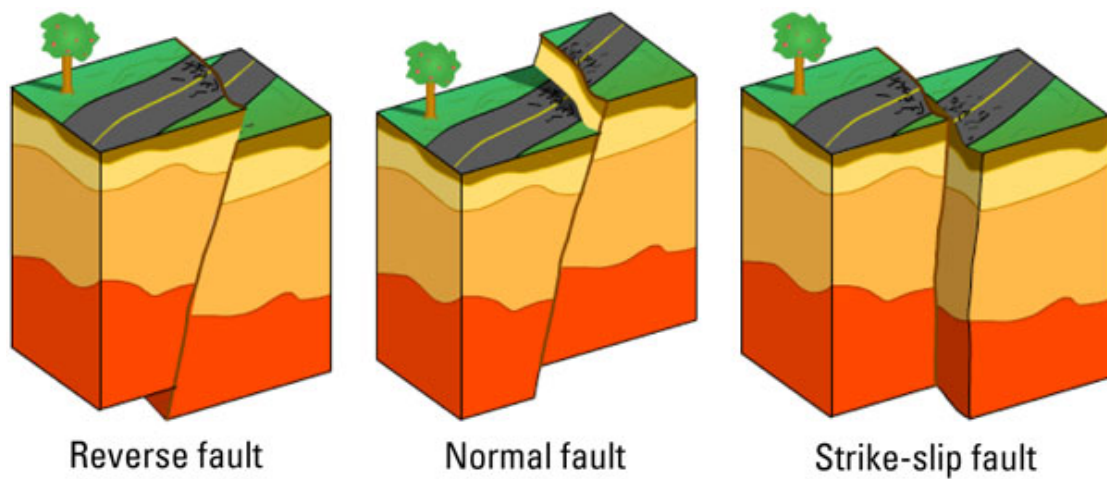


FIGURE 2.8. A cartoon demonstration of Reverse, Normal and Strike-slip Fault. (Gibbons, 2009)

By using this source moment tensor, we can calculate displacements of geophones by P-wave in xz-plane (Figure 2.9). The shape of our calculated P-wave radiation pattern is identical to that by Aki and Richards (1980). We also get an identical match when we calculate the S-wave (Figure 2.9).

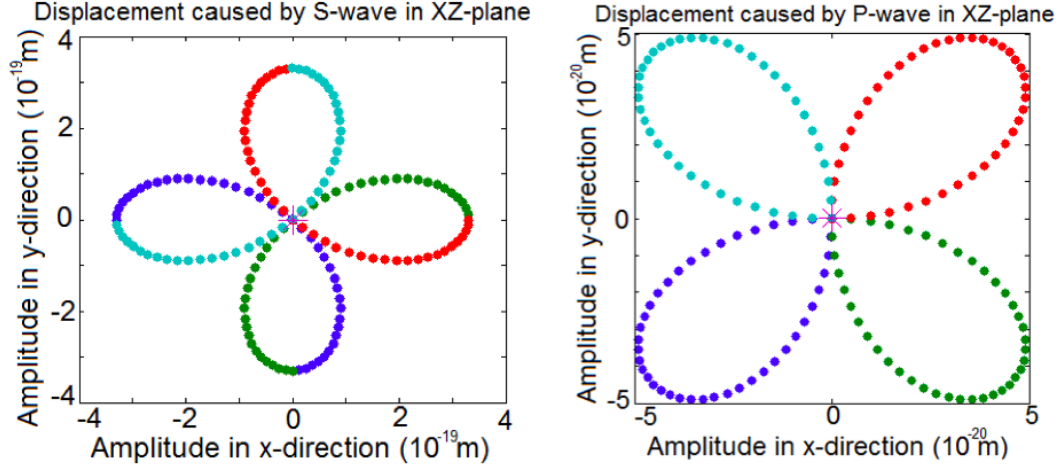


FIGURE 2.9. Displacement caused by P-wave and S-wave in XZ-plane respectively. Blue dots represent that the displacement when the geophone locates at $x > 0$ and $z > 0$. Green dots represent the displacement the displacement when the geophone locates at $x < 0$ and $z > 0$. Red dots represent the displacement the displacement when the geophone locates at $x < 0$ and $z < 0$. Cyan dots represent the displacement the displacement when the geophone locates at $x > 0$ and $z < 0$.

Two different receiver arrays are used to calculate synthetic seismograms (Figure 2.10) using a double couple source (Figure 2.11 to Figure 2.14). The source-receiver distances for array 1 varies from 140 m (450 ft) to 300 m (1000 ft), and that for array 2 is varies from 300 m (1000 ft) to 400 m (1300 ft). With different source-receiver distances, the first arrival of P-wave, S-wave, and S - P wave for the synthetic seismograms are different (Figure 2.11 to Figure 2.12). The ones that source-receiver distance is longer (Figure 2.12) has larger arrival times than the shorter ones (Figure 2.11). Meanwhile, the amplitudes of displacement and velocity in the ones that source-receiver distance is shorter (Figure 2.11) are bigger than the longer ones (Figure 2.12).

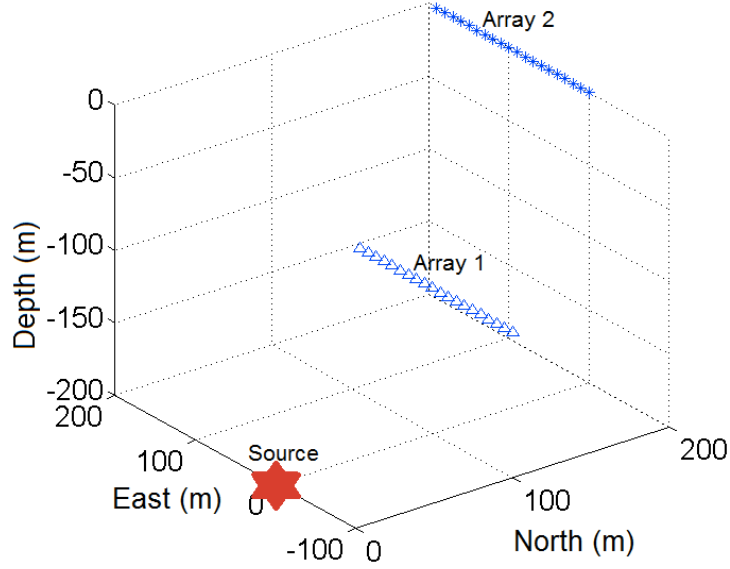


FIGURE 2.10. Arrangement3: source-receiver geometry used for synthetic seismograms. The red star represents the seismic source. Array 1 (shown by triangles) and Array 2 (shown by stars) are linear which represent receivers. The source is located at $x = y = 0$ and a depth of 200 m. Both array 1 and array 2 represent vertical sets of receivers. The minimum source to array 1 distance is about 140 m. The minimum source to array 2 distance is about 300 m.

Our calculation indicate that the amplitude of the intermediate-field terms is of size $1/3$ of the amplitude of contributed by the far-field terms (Figure 2.12 and Figure 2.13). Thus, the intermediate-field terms are significant and should be taken into account by using the rock parameters under this condition. I will take about the quantity of significant in the noise effects part, i.e. which number is called significant in microseismic events.

Our calculation indicate that the amplitude of near-field term contributes almost 0 of the amplitude of far-field terms when the source-receiver distance is about 1000 ft which is the source-receiver distance in microseismic analysis (Figure 2.13 and Figure 2.14). The source-receiver geometry in microseismic analysis is from 1000 ft to 2000 ft in the field. The seismograms with only near-field terms for array 1 (the source-receiver distance is about 450 ft) in the scale of maximum amplitude of the far-field terms are several straight lines. It means that even when the source-

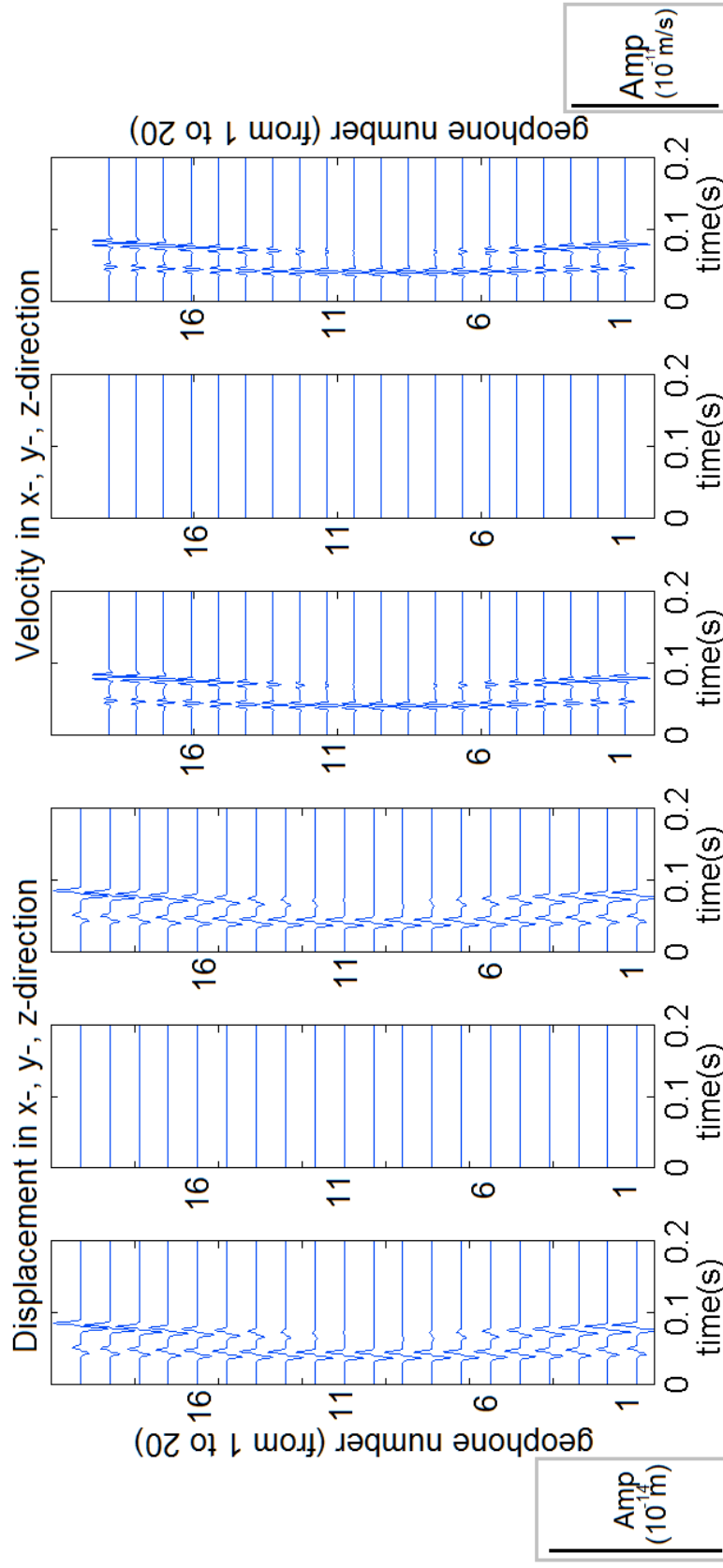


FIGURE 2.11. Seismogram represents far-field displacement and far-field velocity with Array 1. The moment tensor used for this seismogram is double couple.

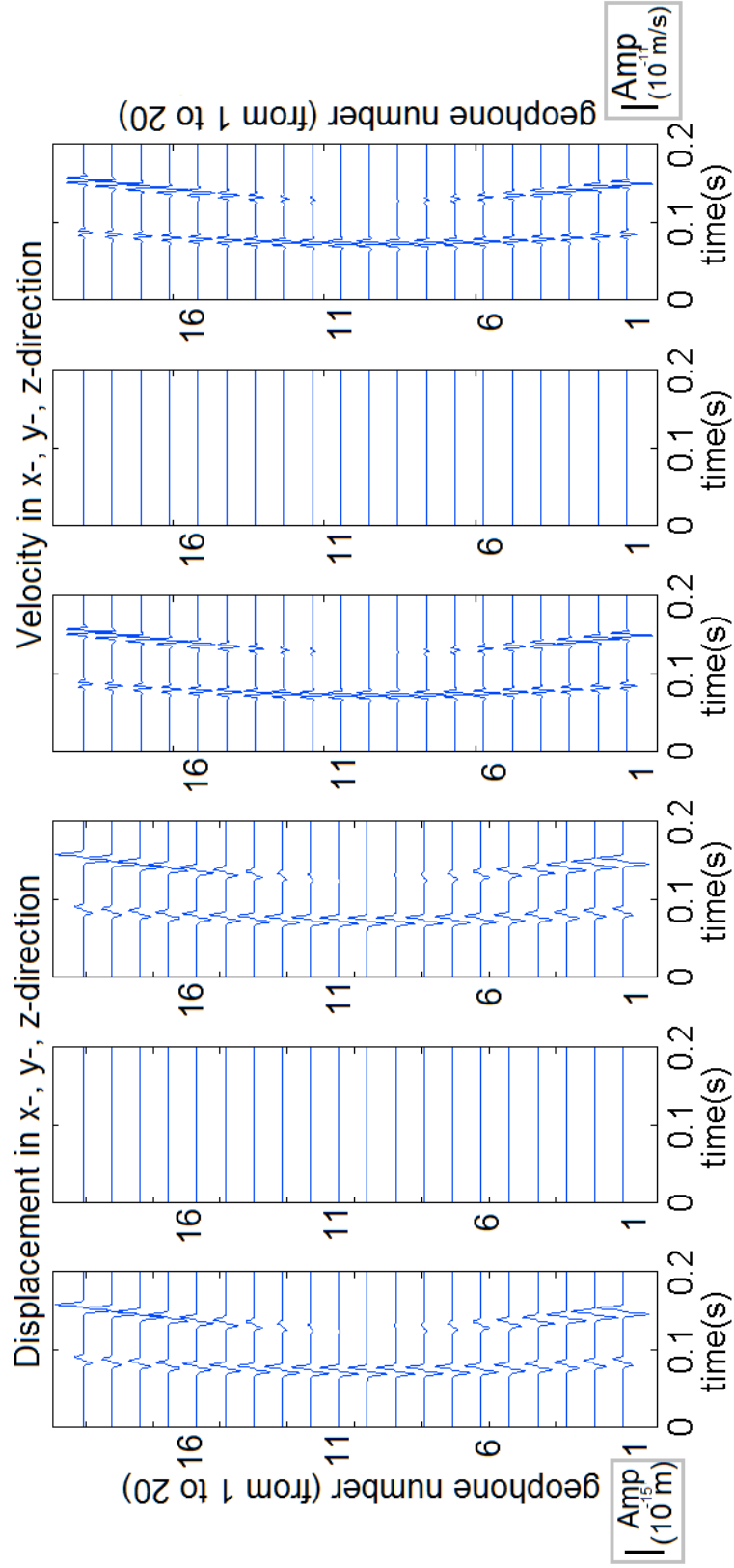


FIGURE 2.12. Seismogram represents far-field displacement and far-field velocity with Array 2. The moment tensor used for this seismogram is double couple.

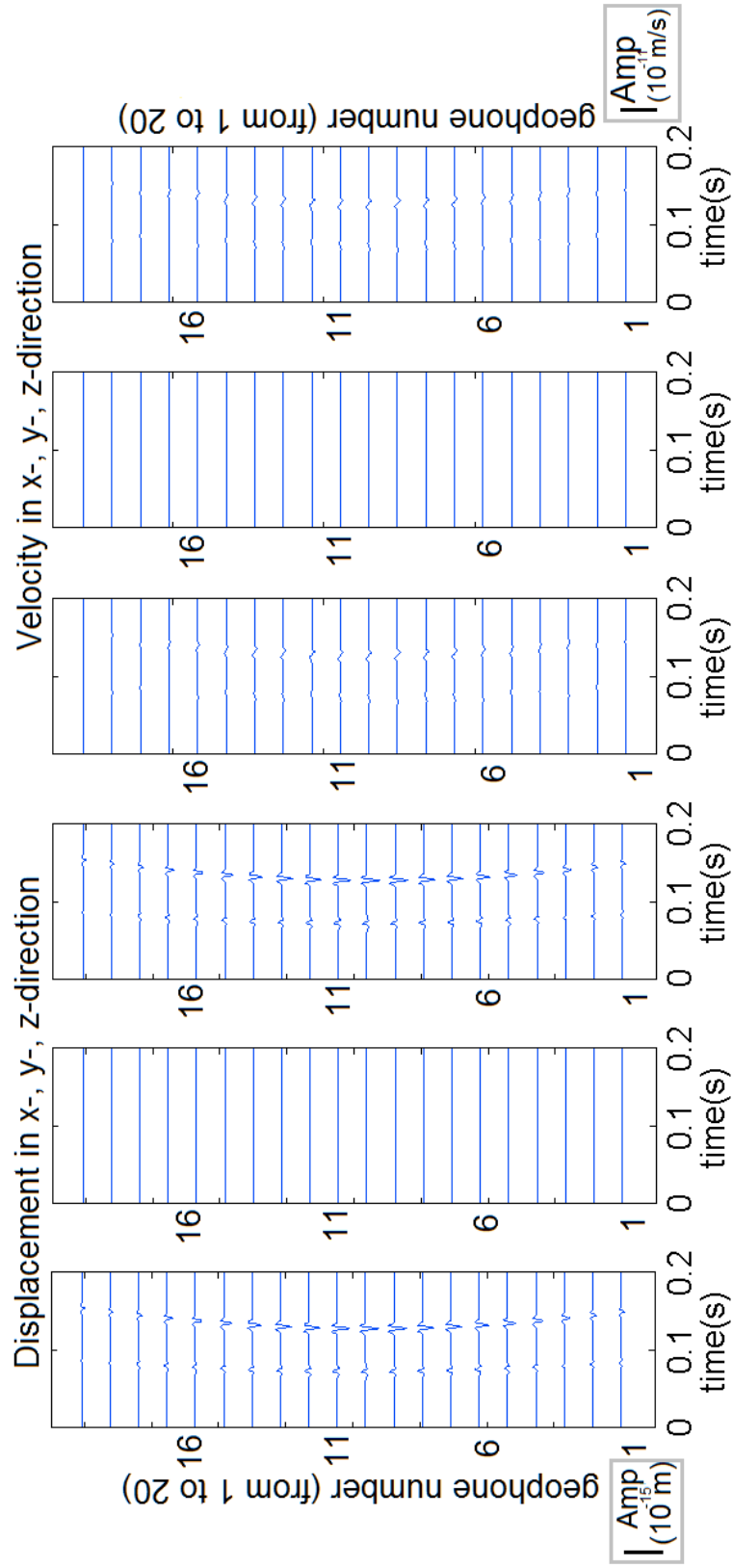


FIGURE 2.13. Seismogram represents intermediate-field displacement and intermediate-field velocity with Array 2. The moment tensor used for this seismogram is double couple.

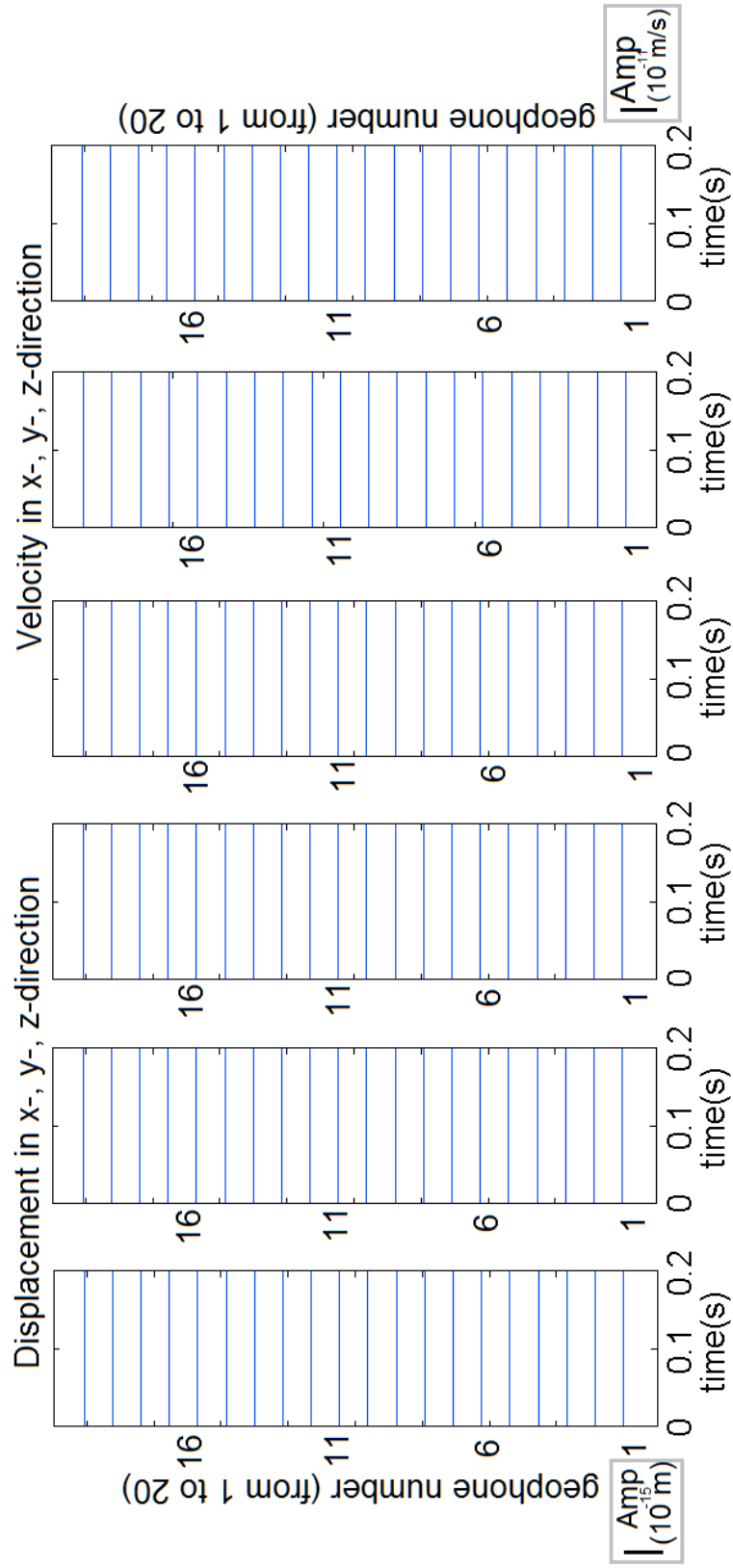


FIGURE 2.14. Seismogram represents near-field displacement and near-field velocity with Array 2. The moment tensor used for this seismogram is double couple.

receiver distance is less than 450 ft, the near-field terms can be ignored. To quantify the numbers, when the source-receiver distance is about 300 ft, the near-field term contributes about 1/20 of far-field terms under this condition. In another word, near-field term can be ignored in microseismic analysis.

2.2.3 Intermediate-field and near-field effects

In the displacement equation above (Equation 2.10), the first term is called near-field term, the second term is called intermediate-term caused by P wave (the coefficient \vec{A}^{IP} is also the same meaning), and the third term is intermediate-term caused by S wave (the coefficient \vec{A}^{IS} is also the same meaning). When the source-receiver distance is short enough, the near-field and intermediate-field terms will have a relatively larger impact on the displacement due to any type of sources. When the source-receiver distance is larger than 1000 ft (approximate 300 m) (Figure 2.13 and Figure 2.14), the near-field and intermediate-field terms effects can be ignored. Figure 2.15 demonstrates the amplitude of the displacement caused by the distance portion of near-field, intermediate-field, and far-field terms. When the source-receiver distance is less than 4 ft (1.2 m), the near-field and intermediate-field terms changed the displacement dramatically; when the source-receiver distance is longer than 300 ft (100 m), the intermediate and near-field terms can be ignored (Figure 2.15). However, this phenomena only considers the source-receiver distance. The amplitude of displacement caused by far-, intermediate-, or near-field terms is also related with density, Young's modular, and Poisson's ratio. The position of the receiver also affects the amplitude of displacement (Figure 2.1 angles θ and ϕ)

When the source receiver distance is less than 1000 ft, the amplitude of first arrival of P wave or S wave in the seismogram increases including intermediate-field terms. When the source receiver distance is about 400 ft, the amplitude of

the first arrival of P-wave and S-wave increase about 1.6 of far-field terms only after we take intermediate-terms into consideration (Figure 2.16). There is also an accompanying additional pulse in the S wave arrival, embedded within the most completely calculated seismogram (Figure 2.16).

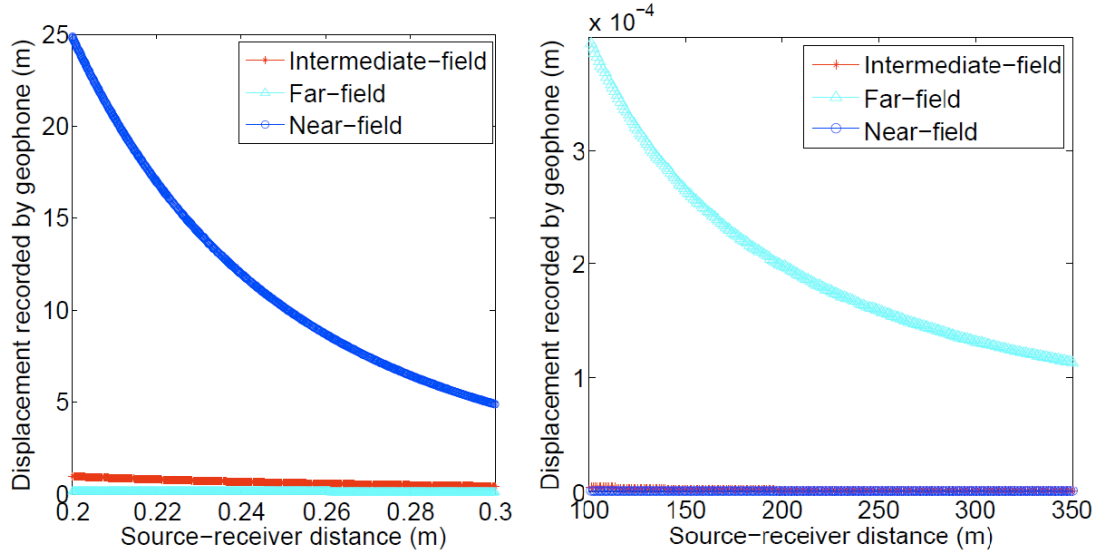


FIGURE 2.15. The amplitude of the displacement only consider the source-receiver distance caused by near-field, intermediate-field, and far-field terms, at (a) a source-receiver distance of between 0.2 m to 0.3 m, and at (b) the source-receiver distance of between 100 m to 350 m.

2.2.4 Noise effects

The treatment well is an adverse environment in which to obtain analyzable seismic data. Microseismic events, created by well-treatment fracturing, are the desired seismic signals. All the other signals are considered as noise (Boroumand and Bland, 2012). Microseismic noise can be divided into coherent noise and incoherent noise. Incoherent noise is unpredictable in time and space (Boroumand and Bland, 2012). Typically incoherent noise is associated with the movement of subsurface fluid or gas, and temperature variations, fluid or gas flow travelling within a borehole and random noise from electronics. On the other hand, coherent noise can be coherent in time (e.g. a pump that emits a regular pulse train,

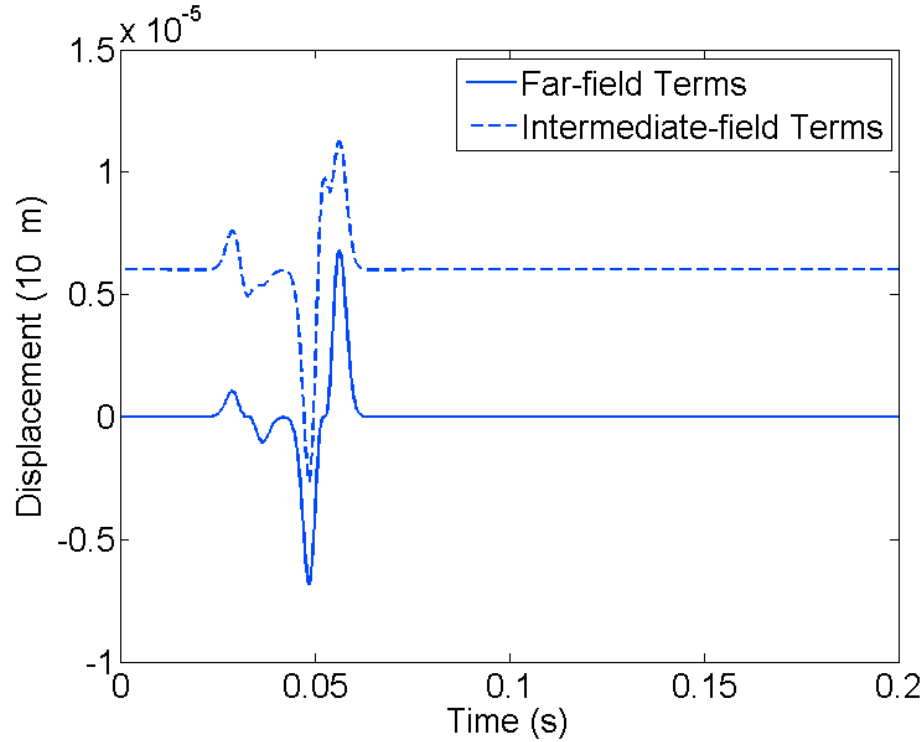


FIGURE 2.16. A synthetic seismogram from a 400 ft source-receiver geometry. The blue line represents a synthetic seismogram only contains far-field terms. The red line represents a synthetic seismogram contains both far-field and intermediate-field components.

resonances in geophone clamping, AC power-line hum, clock-related noise in electronics) (Boroumand and Bland, 2012).

Understanding the effect of noise and the treatment of noise on event-location and moment tensor inversion accuracy is important as noise-related positioning errors can affect the final microseismic interpretation (Warpinski et al., 1995). The challenge is how to induce the noise into our simulation. One way is to study the actual noise from experiments and apply them in simulation.

Several approaches exist to assess the effect of noise. Warpinski et al. (1995) obtain an experimental noise dataset with both coherent and incoherent component. They apply frequency-specific filters to reduce the noise but avoided distorting the signal of interest. Excessively aggressive filtering can result in an erroneous interpretation of the waveform. A comparison is between event locations computed

using unfiltered and filtered data. Additionally, a series of random and coherent noise signals are added to the unfiltered seismic signals and the microseismic events are relocated. The effect of noise on event-location accuracy is observed and evaluated. Warpinski et al. (1995) indicate that understanding the effect of noise and the treatment of noise on event-location accuracy is important as noise-related positioning errors can affect the final microseismic interpretation.

Rietsch (2000) considers the noise component into his software SeisLab 2.01 to generate a seismic dataset. Now we turn our attention on how to apply the noise in our simulation. First, following Rietsch (2000), I use a Gaussian random function and a uniform random function to add coherent and incoherent noise into a synthetic seismogram associated with hydraulic fracture. Second, using the same double-couple and the same rock, the seismograms are shown in Chapter 2 section 2.2.2, the seismograms become different as we including noise, see Figure 2.17. Before the signal propagate to the receiver, the seismogram shows a straight line without noise and some curve with noise. The noise also makes the amplitude of the signal in seismogram increase or decrease.

Boroumand and Bland (2012) also cite that the signal to noise ratio in microseismic events is from 1.2 to 3 which means that the minimum noise contributes about 1/20 of the seismogram. Based on the noise, we estimate when the intermediate-field terms or near-field term dedicates more than 1/20 of the far-field terms, they are significant. Considering intermediate-field terms, the signal to noise ratio will enhance. We can improve the precision of source mechanism analysis for microseismic events.

2.3 Seismic Waves in a Homogeneous and Anisotropic Medium

Real media treated by hydraulic fracturing are generally anisotropic so that if synthetic seismograms can help us understand the real world, they should also

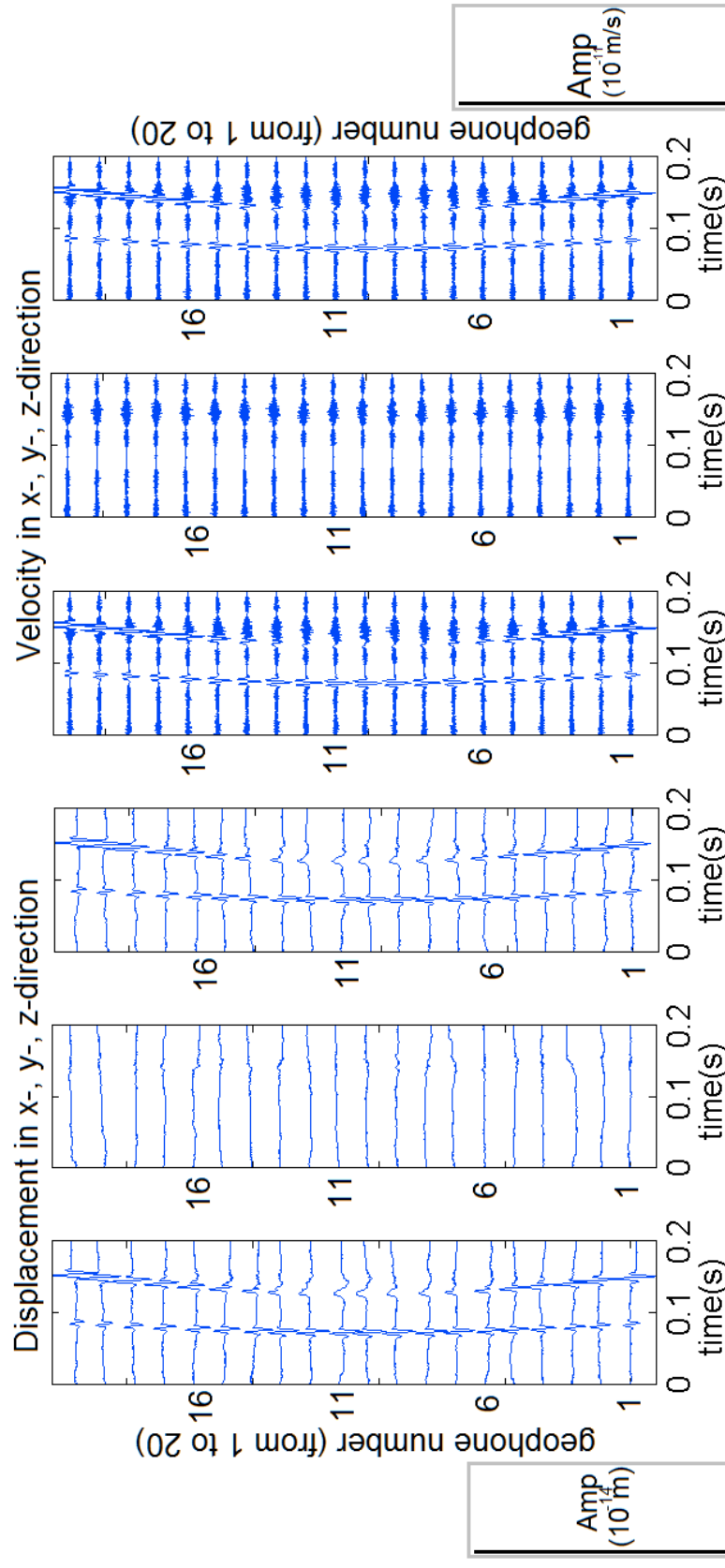


FIGURE 2.17. Seismogram represents total displacement and total velocity with 10% noise from Array 2. The frequency of the noise is 5 Hz, 12 Hz, and 17 Hz. The displacement is the integral of velocity.

incorporate the effects of anisotropy. As previously introduced, microseismic monitoring is a valuable tool to map the hydraulic fracture (Warpinski et al., 2001). This technology is an application of earthquake seismology in which compressional (P) and shear (S) arrivals are detected at some number of receivers and the location of the microseism is deduced by means of ray tracing or other travel-time estimates through some known velocity structure (Albright, 1982). The uncertainty associated with the microseismic location has two primary components. The first is the ability to accurately detect the P and S arrivals; the second is to characterize the velocity structure. The logging tools routinely obtain the velocity along the axis of the borehole, which is the vertical velocity in most wells in which they are commonly run. Most sedimentary rocks exhibit a significant degree of transverse anisotropy in their velocities as a result of layering, mineralogy, and natural fracturing (Thomsen, 1986). As a result, the vertical velocities that are routinely obtained with wellbore sonic logs are inappropriate for microseismic mapping; the direct usage of these velocities can result in large errors in the location of the microseisms. Thomsen (1986) shows how an assumption of weak anisotropy can be used to simplify the complex system of equations that would result for the general case of transverse anisotropy. Under the conditions of weak transverse anisotropy, the formation can be characterized by only a vertical velocity and horizontal velocity.

Here is a literature example of how such method been modified and applied. Warpinski (2009) uses anisotropy information based on core measurements given by Thomsen (1986) in microseismic mapping tests. On many of these tests, the actual perforation or string shot firing time can be accurately measured and used to aid in the construction of the velocity model (Warpinski et al., 2005). They also list a series of measurements of P-wave and S-wave velocities that are made in the tests. Then, they evaluate the importance of anisotropy in determining the accu-

racy of locations of microseismic. They conclude that accurate locations of microseismic events strongly depend on having an adequate velocity structure through the formation traversed by the ray paths. The obvious transverse anisotropy of many reservoir rocks, facets of which are commonly observed in the microseismic data, complicates both the approach used in calculating travel times and the determination of accurate velocities and anisotropy parameters to be used in the analysis. Again, it is inappropriate to directly use the vertical velocities, as measured by dipole sonic logs or VSP surveys, because a velocity structure obtained from vertical velocities will result in large errors in the microseismic location.

Further, Du and Warpinski (2013) apply a numerical algorithm based on the Newton-Raphson method coupled with SVD for calibrating the velocity model used in microseismic fracture monitoring. The method can handle both isotropic and anisotropic velocities by optimizing the independent stiffness coefficients for isotropic and anisotropic media for each layer.

2.3.1 Double couple and compensated linear vector dipole source with vertically symmetric anisotropy

A wave equation, derived under the acoustic medium assumption for P-waves in transversely isotropic media with a vertical symmetry axis (VTI media), though physically impossible, yields good kinematic approximation to the familiar elastic wave equation for VTI media (Alkhalifah, 1998).

For anisotropic and homogeneous media, the stiffness tensor c_{ijkl} can be repre-

sented in a compressed two-index notation:

$$\begin{pmatrix} c_{11} & c_{12} & c_{13} & 0 & 0 & 0 \\ c_{12} & c_{22} & c_{23} & 0 & 0 & 0 \\ c_{13} & c_{23} & c_{33} & 0 & 0 & 0 \\ 0 & 0 & 0 & c_{44} & 0 & 0 \\ 0 & 0 & 0 & 0 & c_{55} & 0 \\ 0 & 0 & 0 & 0 & 0 & c_{66} \end{pmatrix}.$$

In VTI media, $c_{11} = c_{22}$, $c_{13} = c_{23}$, $c_{44} = c_{55}$, $c_{12} = c_{11} - 2c_{44}$. And the P-wave vertical velocity is

$$v_{Pver} = \sqrt{\frac{c_{33}}{\rho}} \quad (2.16)$$

P-wave horizontal velocity is

$$v_{Phor} = \sqrt{\frac{c_{11}}{\rho}} \quad (2.17)$$

S-wave vertical velocity is

$$v_{Sver} = \sqrt{\frac{c_{66}}{\rho}} \quad (2.18)$$

S-wave horizontal velocity is

$$v_{Shor} = \sqrt{\frac{c_{44}}{\rho}} \quad (2.19)$$

In the equations above, ρ is the density of the media. Since the media is homogeneous, the density is constant (Alkhalifah, 2000).

For the displacement in anisotropic and homogeneous media, the following two equations are derived:

$$\begin{cases} \frac{\partial^2 u_x}{\partial t^2} = c_{11} \frac{\partial^2 u_x}{\partial x^2} + 2c_{13} \frac{\partial^2 u_z}{\partial x \partial z} + c_{13} \frac{\partial^2 u_x}{\partial z^2} \\ \frac{\partial^2 u_z}{\partial t^2} = c_{33} \frac{\partial^2 u_z}{\partial z^2} + 2c_{13} \frac{\partial^2 u_x}{\partial x \partial z} + c_{13} \frac{\partial^2 u_z}{\partial x^2} \end{cases} \quad (2.20)$$

(Alkhalifah, 1998)

To calculate the seismograms in the anisotropic media, the known parameters are density, vertical P-wave velocity, horizontal P-wave velocity, vertical S-wave velocity, and horizontal S-wave velocity (Table 2.3).

From the equations 2.16 to 2.19, we can calculate c_{11} , c_{33} , and c_{13} . Then we use Equation 2.10 and horizontal velocity to calculate the seismograms in isotropic medium and use finite difference (Equation 2.20) to calculate the displacement in vertical direction in anisotropic medium (Figure 2.18).

TABLE 2.3. The rock parameters used to calculate the seismograms in anisotropic medium (Warpinski, 2009)

Density (g/cm^3)	2.50
Vertical P-wave velocity (km/s)	3.2005
Vertical S-wave velocity (km/s)	1.5240
Horizontal P-wave velocity (km/s)	4.2672
Horizontal S-wave velocity (km/s)	2.2860

2.3.2 Noise effects

Noise is added into the seismogram in anisotropic medium in velocity. The displacement is integrated from the velocity. The new seismogram is as Figure 2.19 displayed.

From the field data analysis in Barnett Shale Formation, the noise in microseismic events associated with hydraulic fracture is usually low frequency noise (less than 33 Hz) (Warpinski et al., 1995). The frequency is concentrated at values of 5, 7, 12, 17, and 23 Hz.

2.4 Conclusions

The source-receiver distance in field condition is often around 1000 ft (Cipolla and Wright, 2000). In my study, I focus on the source-receiver distances up to 1000 ft. From all the seismograms shown previously, we see that amplitudes created by the intermediate-terms in the synthetic seismograms are about 1/3 of far-field terms, and the near-field terms are less than 1/20 of far-field terms. The results indicate that the intermediate-field terms are important when the source-receiver distance is around 1000 ft, and the near-field terms can be ignored. I also calculate the shortest source-receiver distance for which the intermediate-field effects can be

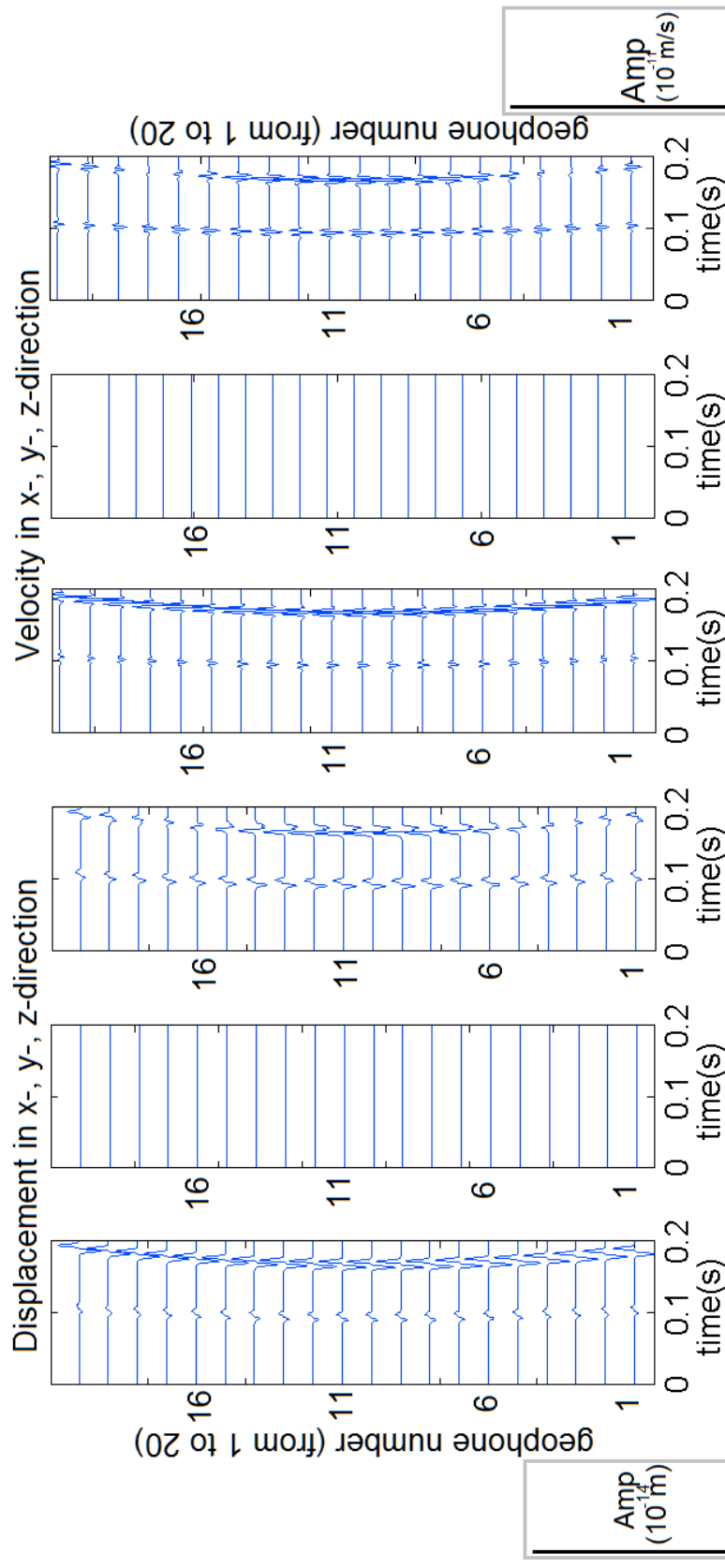


FIGURE 2.18. Seismogram represents total displacement and total velocity from Array 2.

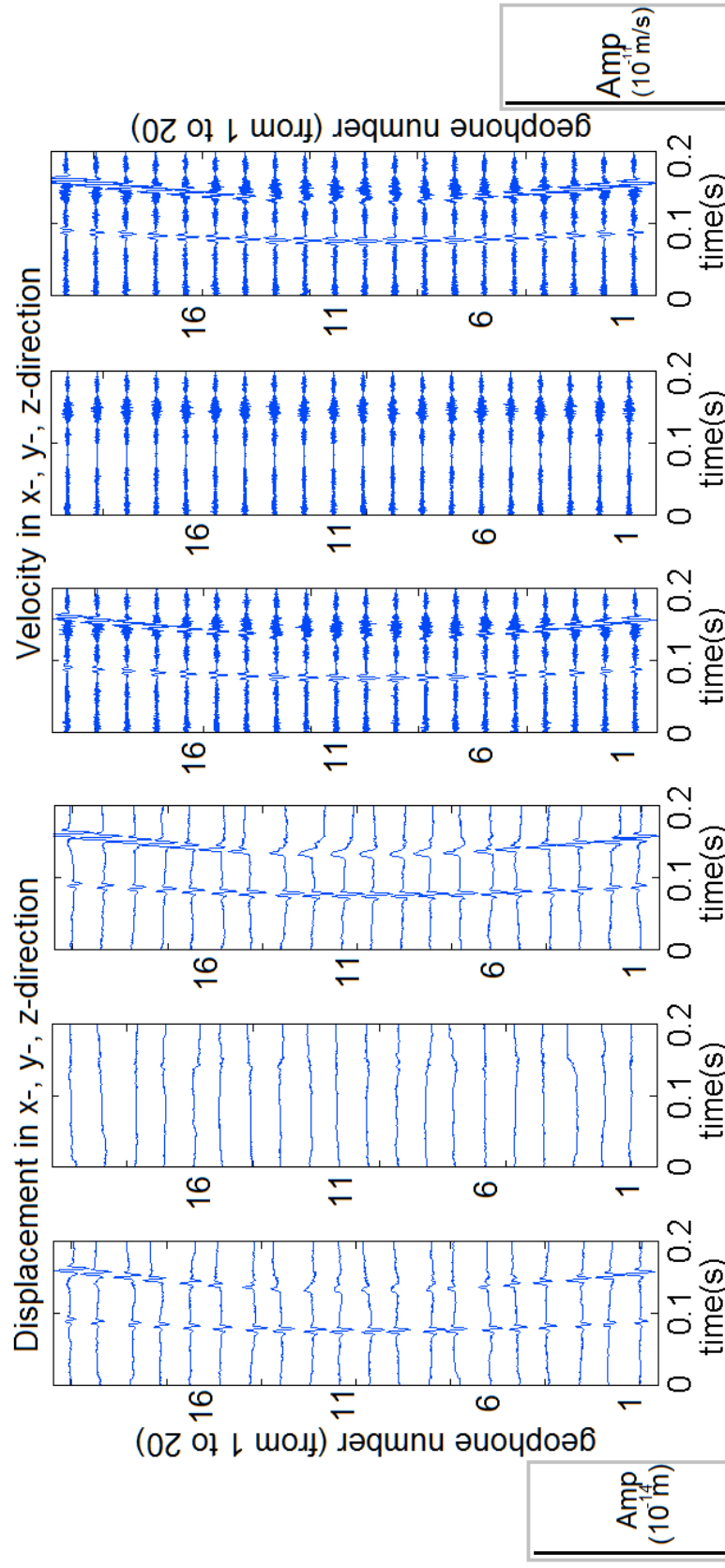


FIGURE 2.19. Seismogram represents total displacement and total velocity plus 10% noise from Array 2.

ignored based on the noise effect in the field. When the magnitude of the noise is the same as for the intermediate-signal, I say that the intermediate-field effect can be ignored, which occurs at distance of 6700 ft for the parameters used in this study. When take noise into the synthetic seismograms, there is distortion in the seismogram as expect.

Chapter 3

Source Mechanisms during Hydraulic Fracturing

3.1 Introduction

The physics of seismic sources is a major research topic in seismology. The approximation of seismic sources by a model of equivalent forces that correspond to linear wave equations neglecting non-linear effects in the near source region is the common approach (Geller, 1976; Aki and Richards, 1980). The equivalent forces are defined as producing displacements in an infinite medium that are identical to those from the actual forces of the physical process at the source. The equivalent forces are determined from recorded seismograms which contain information about the source, path, and distortions at the vicinity of the receiver (Jost and Herrmann, 1989). The principle problem in source studies is the isolation of the source effect by correcting for the instrument and path. The classic method of describing seismic sources is by their strength and fault plane solution (Honda, 1962). In 1970s, moment tensors are introduced for calculating the displacement caused by a fault (Gilbert, 1970). Nowadays, seismic moment tensors have been widely used to describe seismic sources in both earthquakes and hydraulic fracturing.

Information about hydraulic fracturing process has to be obtained from the analysis of seismic waves radiated from the source. Unfortunately, dynamic problems of fracture mechanics lead to complex boundary value problems in elastodynamics, which are not solvable in general (Kostrov and Das, 1988). Instead, the kinematic description of displacement jumps along the fracture surface as a function of position and time may permit the inverse problem formulation. The moment tensor describes the equivalent forces exerted on a fracture. The equivalent forces can

be correlated to physical source models like tensile and shear (Jost and Herrman, 1989). Typically, there are three types of elastodynamic sources commonly used in decomposition of a moment tensor (Julian et al., 1998): isotropic, double couple (DC), and compensated linear vector dipole (CLVD). A moment tensor is a 3x3 symmetric matrix. It is possible to calculate the principal moment tensor and express the moment tensor in the principal coordinate system. We can always begin

$$\begin{aligned}
& \text{with a principal moment tensor } \begin{pmatrix} M_1 & 0 & 0 \\ 0 & M_2 & 0 \\ 0 & 0 & M_3 \end{pmatrix}, \text{ and decompose it as follows} \\
& \begin{pmatrix} M_1 & 0 & 0 \\ 0 & M_2 & 0 \\ 0 & 0 & M_3 \end{pmatrix} = \begin{pmatrix} \frac{M_1+M_2+M_3}{3} & 0 & 0 \\ 0 & \frac{M_1+M_2+M_3}{3} & 0 \\ 0 & 0 & \frac{M_1+M_2+M_3}{3} \end{pmatrix}^{ISO} \\
& + \begin{pmatrix} \frac{M_1-M_3}{2} & 0 & 0 \\ 0 & 0 & 0 \\ 0 & 0 & \frac{M_1-M_3}{2} \end{pmatrix}^{DC} + \begin{pmatrix} \frac{M_1-2M_2+M_3}{6} & 0 & 0 \\ 0 & \frac{-M_1+2M_2-M_3}{3} & 0 \\ 0 & 0 & \frac{M_1-2M_2+M_3}{6} \end{pmatrix}^{CLVD} \\
& \tag{3.1}
\end{aligned}$$

The first part is called the isotropic (ISO), the second is called the double couple (DC), and the last one is called the compensated linear vector dipole (CLVD). It is noticeable that in the third part, M_{11} equals M_{33} . The isotropic part represents changes in volume like an explosion or an implosion. The double couple part represents pure shear fracture, which usually approximate earthquakes (Lee et al., 2002). CLVD represents the tensile cracks, which is commonly associated with volcanoes and volcanic unrest (Shuler et al., 2013).

There are various methods for moment tensor inversion. The inversion can be done in the time domain or frequency domain. For example, one may use free os-

cillations, surface waves, body waves, and seismogram components separately or in combined form for moment tensor inversion (Gilbert and Dziewonski, 1975; McCowan, 1976, Menduguren, 1977; Stump and Johnson, 1977, Ward, 1980; Backus, 1977).

3.2 A Source Mechanism Study for a Homogeneous and Isotropic Medium

Microseismic mapping is a valuable tool in understanding the efficiency of hydraulic fracturing treatments. Determination of event locations and magnitudes leads to estimations of the geometry of the fracture zone and dynamics of the fracturing process. With sufficient resolution, the hypocenters may even reveal failure planes or other underlying structures controlling the distribution of events. Microseismic mapping has proven to be a valuable technology for understanding hydraulic-fracture growth and behavior. The seismic waves generated by the microseismic event may also contain information with potential value for understanding the reservoir, natural fractures, stress state, and fracturing mechanisms (Warpinski and Du, 2010).

Extracting information from the microseismic data requires the use of a source model, which in its most general form is represented by a symmetric moment tensor having six components. Difficulties arise when attempting to invert for the components of the moment tensor if only a single monitor well is available, but in principle the full moment tensor can be extracted for multiple monitor wells. The primary information derived consists of the slippage-plane orientation, the slip direction, and the moment (strength) of the event. Presumably, these slippages occur on existing planes of weakness, such as natural fractures, bedding planes, or potentially even fracture planes induced by the hydraulic fracture (Warpinski et al., 1998), thus providing information about the reservoir and the process. An

approach for performing the moment-tensor inversion is discussed for both single and multiple monitor wells, along with methods to estimate various parameters. Both synthetic and field examples are provided in section 3.2 to demonstrate what can be extracted from the data set under various conditions.

To implement moment tensor inversion, we use the free software ISOLA. The details of the software and how to use it and changes in the code to adapt it for present problem are provided in the Appendix B.

3.2.1 Moment tensor inversion for synthetic seismograms

We use synthetic seismograms from homogenous and isotropic media without any noise to verify the ISOLA given by Zahradnik and Sokos (2008), a MATLAB GUI for source inversion. The source is a double-couple. ISOLA only considers far-field terms of P-wave and S-wave for the purpose of moment tensor inversion. The input moment tensor and output results are shown in Figure 3.1.

The input moment tensor is what we input into MATLAB code (Chapter 2) to generate synthetic seismograms, and the output result is using the seismograms to obtain moment tensor from ISOLA. Ideally, the input moment tensor should be the same as the output one. Comparing the input moment tensor and the output one, we can get a conclusion whether ISOLA provides acceptable results (Figure 3.1). If we compare the input moment tensor and output results quantitatively, the angular difference is less than 2% (Figure 3.2). In the next step, we use ISOLA to do moment tensor inversion.

As discussed in chapter 2, the intermediate-field terms may strongly affect displacements when the source-receiver distance is less than 1000 ft (Equation 2.10). Therefore, it is reasonable to consider them for moment tensor inversion. We take intermediate-field terms into the inversion algorithm to do moment tensor inversion, and expect the moment tensor inversion is more precise by including the

Moment Tensor Input into Seismogram	Beach Ball (Theoretical)	Moment Tensor Inversion (From ISOLA)
$\begin{pmatrix} 0 & M & 0 \\ M & 0 & 0 \\ 0 & 0 & 0 \end{pmatrix}$ Vertical strike slip fault		
$\begin{pmatrix} 0 & 0 & 0 \\ 0 & -M & 0 \\ 0 & 0 & M \end{pmatrix}$ 45 degree dip slip fault		
$\begin{pmatrix} 0 & 0 & 0 \\ 0 & 0 & -M \\ 0 & -M & 0 \end{pmatrix}$ Vertical dip slip fault		
$\begin{pmatrix} 0 & 0 & M \\ 0 & 0 & 0 \\ M & 0 & 0 \end{pmatrix}$		
$\begin{pmatrix} -M & 0 & 0 \\ 0 & 0 & 0 \\ 0 & 0 & M \end{pmatrix}$		

FIGURE 3.1. The first column shows the input moment tensor to generate the seismogram; the second column shows the theoretical beach-ball of the corresponding moment tensor; the third column represents the moment tensor inverted by ISOLA.

intermediate-field terms. The output moment tensors generated by considering intermediate-field terms and far-field terms give about 2% better results comparing with the ones only considering far-field terms (Figure 3.2). These three moment

Seismogram	Moment tensor	Strike (°)	Dip (°)	Rake (°)
Theoretical	$\begin{pmatrix} 0 & M & 0 \\ M & 0 & 0 \\ 0 & 0 & 0 \end{pmatrix}$	0	90	0
Far-field terms		183	89	0
Far- and intermediate-field		180	89	0
Theoretical	$\begin{pmatrix} 0 & 0 & 0 \\ 0 & -M & 0 \\ 0 & 0 & M \end{pmatrix}$	0	45	90
Far-field terms		0	44	89
Far- and intermediate-field		0	44	90
Theoretical	$\begin{pmatrix} 0 & 0 & 0 \\ 0 & 0 & -M \\ 0 & -M & 0 \end{pmatrix}$	0	90	90
Far-field terms		179	89	90
Far- and intermediate-field		180	89	90

FIGURE 3.2. The strike, dip, and rake angles given initially and calculated numerically are given. The word ‘theoretical’ in the first column means that the strike, dip, and rake angles correspond to the fault caused by the moment tensor. ‘Far-field’ terms means that we use the synthetic seismograms that only consider far-field terms for moment tensor inversion. ‘Both’ in the first column means that the inversion considers both far-field and intermediate-field terms.

tensors represent the three typical types of double-couple. The source-receiver geometry is shown in array 2 of Figure 2.10 (also see later Figure 3.3).

After comparing theoretical and the computed moment tensors generated by a double-couple, we also compare the same thing for CLVD mechanism. The double-couple is a pure shear and is not the type of loading expected during hydraulic fracturing. We mainly expect CLVD and isotropic mechanisms during the treatment due to fracture opening. Figure 3.3 illustrates the CLVD, theoretical beach-ball, and numerically calculated results. The synthetic seismograms only contain the far-field terms for displacement calculation (Equation 2.10).

The output beach ball is different from the input one (Figure 3.3). The source mechanism from the synthetic seismograms contains more double-couple part. However, to quantitatively describe the moment tensor inversion, we can see the







Moment tensor	Theoretical Beach-ball	Output of original ISOLA
$\begin{pmatrix} M & 0 & 0 \\ 0 & -2M & 0 \\ 0 & 0 & M \end{pmatrix}$		
$\begin{pmatrix} M & 0 & 0 \\ 0 & M & 0 \\ 0 & 0 & -2M \end{pmatrix}$		
$\begin{pmatrix} -2M & 0 & 0 \\ 0 & M & 0 \\ 0 & 0 & M \end{pmatrix}$		

FIGURE 3.3. The first column is the input moment tensor to generate the seismogram; the second column is the theoretical beach-ball of the corresponding moment tensor; the third column represents the moment tensor inversion calculated numerically.

CLVD is taking more than 90% in the whole results in the above three cases. The reason is that the way to draw the beach ball in ISOLA only displays double-couple. Then we use the output data from ISOLA and Generic Mapping Tools (GMT) to illustrate the focal mechanism. The code to display beach ball of CLVD is in Appendix B. The modified inversion results and the theoretical ones are in Figure 3.4. A comparison of the output beach ball and the theoretical one, we can see the two results are similar with each other. We can use GMT to display beach ball from CLVD sources.

We also use the synthetic seismograms including both intermediate-field terms and far-field terms to do moment tensor inversion. The output results show no difference with the ones in Figure 3.4.

Different seismic moment tensors predict different relative amplitudes for P- and S-wave arrivals. The intermediate-field terms also have a significant amplitude contribution when the source-receiver distance is less than 1000 ft (300 m), which is the distance of microseismic events associated with hydraulic fracture. To see









Moment tensor	Theoretical Beach-ball	Output of GMT (ISOLA)
$\begin{pmatrix} M & 0 & 0 \\ 0 & -2M & 0 \\ 0 & 0 & M \end{pmatrix}$		
$\begin{pmatrix} M & 0 & 0 \\ 0 & M & 0 \\ 0 & 0 & -2M \end{pmatrix}$		
$\begin{pmatrix} -2M & 0 & 0 \\ 0 & M & 0 \\ 0 & 0 & M \end{pmatrix}$		
$-\begin{pmatrix} M & 0 & 0 \\ 0 & M & 0 \\ 0 & 0 & -2M \end{pmatrix}$		

FIGURE 3.4. The first column is the input moment tensor to generate the seismogram; the second column is the theoretical beach-ball of the corresponded moment tensor; the third column is the moment tensor inversion given by GMT using the data given by ISOLA.

the difference between different source-receiver geometry, moment tensor inversion is also done for synthetic seismograms from array 1 and array 3 (Figure 3.5). We get same answers of strike, dip, and rake from double-couple sources as Figure 3.2 demonstrates by using far-field terms only and far-field terms plus intermediate-field terms.

We also use the synthetic seismograms including both intermediate-field terms and far-field terms to do moment tensor inversion for several scenarios, which are considered to investigate the accuracy of including intermediate-field terms into doing moment tensor inversion. The output results show no difference with the ones in Figure 3.4. We can conclude that when the source-receiver distance is less than 300 m, the results of moment tensor inversion improve about 3% by considering intermediate-field terms.

3.2.2 Moment tensor inversion for synthetic seismogram with noise

In microseismic events, the environment is noisy. The average signal to noise ratio is 2 (Boroumand and Bland, 2012). We analyze the field data, get the noise, and add to the synthetic seismograms. Next we use cross correlation and filter to decrease the noise. Figure 3.6 describes that the beach ball from the seismograms with noise. The signal to noise ratio after filters is 10. Figure 3.7 and Figure 3.8 demonstrate that the accuracy of the beach ball and strike, dip, and rake improved by including intermediate-field terms in doing moment tensor inversion.

From this work, it is clear that the intermediate-field terms of displacement (or velocity) in microseisms associated with hydraulic fracturing should be used to invert to get the source mechanisms. The output moment tensor will be more

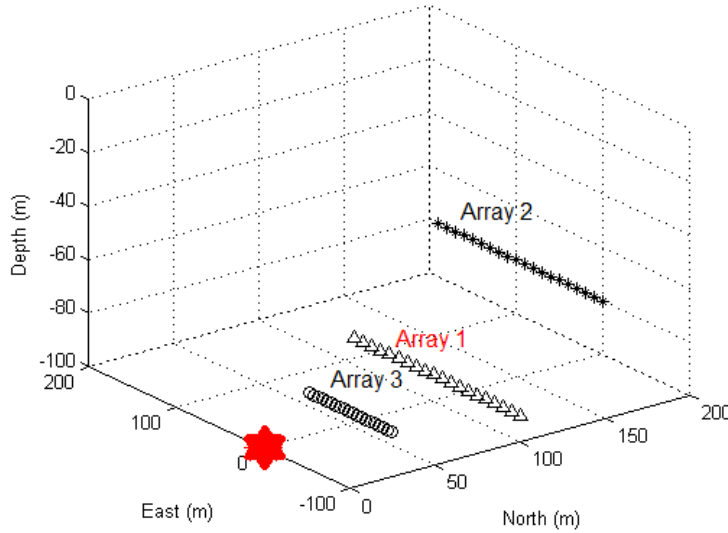


FIGURE 3.5. Source-receiver geometry used for synthetic seismograms. Array 1 (shown by triangles), array 2 (shown by stars), and array 3 (shown by circles) are all linear. The source is located at $x=y=0$ and a depth of 100 m. Array 1 represents a horizontal set of receivers between -100 to 90 m east, located 100 m north and 10 m shallower of the source. Array 2 represents is located between 0-190 m east and includes a 100 m borehole deviation the north and 20 m difference of depth. Receivers are shown every 10 m in array 1 and array 2 in Figure 1. Array 3 represents a horizontal set of receivers between -50 to 45 m east, 50m north, and 5 m shallower of source. Receivers are every 5 m in array 3.

Moment Tensor Input into Seismogram	Beach Ball (Theoretical)	Moment Tensor Inversion (From ISOLA)
$\begin{pmatrix} 0 & M & 0 \\ M & 0 & 0 \\ 0 & 0 & 0 \end{pmatrix}$ Vertical strike slip fault		 Far-field
$\begin{pmatrix} 0 & M & 0 \\ M & 0 & 0 \\ 0 & 0 & 0 \end{pmatrix}$ Vertical strike slip fault		 Far-field + intermediate-field
$\begin{pmatrix} 0 & 0 & 0 \\ 0 & -M & 0 \\ 0 & 0 & M \end{pmatrix}$ 45 degree dip slip fault		 Far-field
$\begin{pmatrix} 0 & 0 & 0 \\ 0 & -M & 0 \\ 0 & 0 & M \end{pmatrix}$ 45 degree dip slip fault		 Far-field + intermediate-field

FIGURE 3.6. The moment tensor, theoretical beach ball, and the output results from ISOLA.

Seismogram	Moment tensor	Strike (°)	Dip (°)	Rake (°)
Theoretical	$\begin{pmatrix} 0 & M & 0 \\ M & 0 & 0 \\ 0 & 0 & 0 \end{pmatrix}$	0	90	0
Far-field terms		182	83	0
Far- and intermediate-field		180	86	0
Theoretical	$\begin{pmatrix} 0 & 0 & 0 \\ 0 & 0 & -M \\ 0 & -M & 0 \end{pmatrix}$	0	45	90
Far-field terms		20	30	116
Far- and intermediate-field		1	41	78

FIGURE 3.7. The beach ball and strike, dip, and rake of DC source from theoretical, far-field terms, and including intermediate-field terms.

reliable than only considering far-field terms of displacement. For the source receiver distance is less or around 1000 ft in microseismic fracture mapping, the intermediate-field terms should be included to get the source mechanisms. By considering intermediate-field terms to do moment tensor inversion, the signal to noise ratio will increase. The seismograms after processing will have more useful information. Another possible reason is that the marginal data in microseismic events. Only one or two arrays are put in the downhole or on the surface to record the events which makes the recording data are only from one or two directions. Thus, the seismograms recorded by geophones in a same array are similar with each other. In doing moment tensor inversion for earthquakes, the stations to records the seismic waves are all over the world, and the amplitudes of P wave and S wave are not as important as doing moment tensor inversion for microseismic events. Under this condition, the amplitude of first arrival of P wave and S wave becomes more important to get a precise moment tensor inversion.

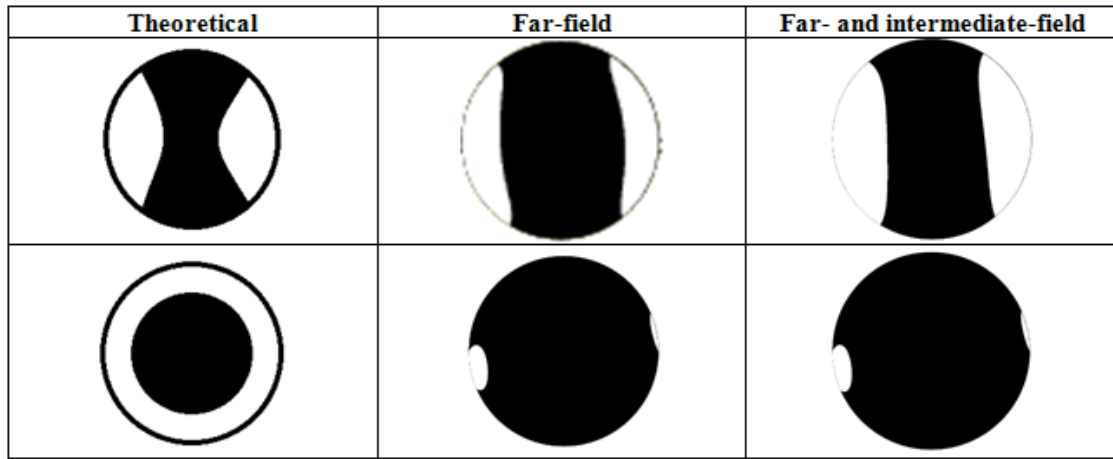


FIGURE 3.8. The beach ball from two different CLVD sources.

Eaton (2009) pointed that the difference of seismograms for two different moment tensors, a double couple and a CLVD source, is relative amplitudes and polarities of first arrival of P wave and S wave. He shows that the upper seismogram and beach

ball are from a double couple source and the lower ones are from a CLVD source. Comparing the upper seismogram and beach ball with lower ones, the difference of the seismograms is the difference of amplitudes and polarities of P wave and S wave.

The non-double-couple modes of failure play an important role in elucidating the underlying failure mechanisms, as they impart information about how the volume of the medium is changing in response to the treatment.

3.3 A Source Mechanism Study for a Homogeneous and Anisotropic Medium

In this section on the study of an anisotropic medium, we use same the same parameters (Chapter 2 section 2.3). When we calculate synthetic seismograms in an anisotropic medium, the horizontal velocity and vertical velocity is different. The horizontal velocities and vertical velocities are the same with Du and Warpinski (2013) using in their paper (refer Table 2.3 in Chapter 2). And these velocities are from field analysis.

When ISOLA inverts the synthetic seismogram to obtain the source moment tensor, ISOLA assumes the medium is isotropic. And we first use horizontal velocity. The location of the source is found using only the horizontal velocity. The equations I use to locate the source are from Equation 3.5 to Equation 3.7.

The arrival times in synthetic seismograms for the anisotropic medium is as follows.

$$t_x = \frac{x}{v_{P_horizontal}} \quad (3.2)$$

$$t_y = \frac{y}{v_{P_horizontal}} \quad (3.3)$$

$$t_z = \frac{z}{v_{P_vertical}} \quad (3.4)$$

If we use horizontal velocity to calculate the location of the source, its position is as follows.

$$x' = v_{P_horizontal} \times t_x = v_{P_horizontal} \times \frac{x}{v_{P_horizontal}} = x \quad (3.5)$$

$$y' = v_{P_horizontal} \times t_y = v_{P_horizontal} \times \frac{y}{v_{P_horizontal}} = y \quad (3.6)$$

$$z' = v_{P_horizontal} \times t_z = v_{P_horizontal} \times \frac{z}{v_{P_vertical}} \neq z \quad (3.7)$$

In the equations above, t_x , t_y , and t_z represent the time of first arrival of P wave; x , y , and z represent the real location of the source; x' , y' , z' represent the calculate location of the source; $v_{P_horizontal}$ and $v_{P_vertical}$ represent horizontal and vertical velocity of P wave; $v_{S_horizontal}$ and $v_{S_vertical}$ represent horizontal and vertical velocity of S wave.

As we can see from the Equation 3.5 to Equation 3.7, the calculated horizontal position of the source is the same as the real location of the source; the calculated vertical position of the source is different than real location of the source (i.e. the depth of the source is not correct when we use the seismograms to locate the source). The error in the position of the source will probably cause the an inaccurate moment tensor inversion.

We use the calculated source location and the horizontal velocity model to carry out moment tensor inversion from the synthetic seismogram and to find out how the anisotropy of the medium affects the result of moment tensor inversion.

Meanwhile, we also want to find out that the improvement by considering intermediate-field terms to do moment tensor inversion. Four different cases are discussed: moment tensor inversion by considering only far-field terms, both far-

Strike (°)	Dip(°)	Rake (°)	Beach Ball
0	45	90	
7	45	97	
6	45	97	
18	65	111	
5	46	86	

FIGURE 3.9. The beach ball of normal fault. The horizontal velocity of the formation is used for velocity model. The second row is the theoretical strike, dip, rake, and beach ball of a normal fault. The third row represents moment tensor inversion of synthetic seismograms considering only considering far-field terms. The fourth row represents moment tensor inversion of synthetic seismograms considering far-field terms and intermediate-field terms. The fifth row represents moment tensor inversion of synthetic seismograms with 10% noise only considering far-field terms. The sixth row represents moment tensor inversion of synthetic seismograms with 10% considering far-field terms and intermediate-field terms.

field and intermediate-field terms for synthetic seismograms, and those two for synthetic seismograms with microseismic noise.

Figure 3.9 demonstrates that how the anisotropy affects the moment tensor inversion if we use horizontal velocity to analyze the source mechanism. The inaccurate of the moment tensor inversion will increase compare with the one without anisotropy effects. The reason is that the location and the velocity model is not exactly with the real one. Considering intermediate-field terms will improve the accurate of source mechanism.

If we use vertical velocity, the location of the source is as follows.

$$x' = v_{P_vertical} \times t_x = v_{P_vertical} \times \frac{x}{v_{P_horizontal}} \neq x \quad (3.8)$$

$$y' = v_{P_vertical} \times t_y = v_{P_vertical} \times \frac{y}{v_{P_horizontal}} \neq y \quad (3.9)$$

$$z' = v_{P_vertical} \times t_z = v_{P_vertical} \times \frac{z}{v_{P_vertical}} = z \quad (3.10)$$

All the parameters in Equation 3.8 to 3.10 have the same meaning with Equation 3.2 to 3.7. The vertical velocity of the media is set to do moment tensor inversion. The results are shown from Figure 3.10.

Figure 3.10 demonstrates that how the anisotropy affects the moment tensor inversion if we use vertical velocity to analyze the source mechanism. The inaccuracy of the moment tensor inversion will increase compare with the one without anisotropy effects and even with using horizontal velocity one. The reason is that the horizontal location is more important than the location of the source in depth. Considering intermediate-field terms will improve the accurate of source mechanism.

Comparing the results in Figure 3.9 and Figure 3.10 with theoretical data, it is obvious that the moment tensor inversion considering intermediate-terms is more precise. When we use horizontal velocities to calculate the moment tensor inversion, the moment tensor inversion is more accurate. The reason is that the location of the source is only changed in depth. At the same time, the program to do moment tensor is sensitive for the horizontal location of the source instead of the depth of the source. When we use vertical velocities to do moment tensor inversion, we get the results the angels of the strike, dip and rake change more than 25% with


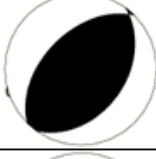
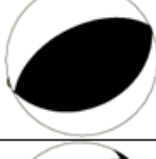
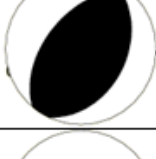
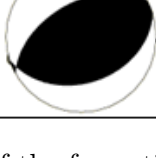
Strike (°)	Dip(°)	Rake (°)	Beach Ball
0	45	90	
45	50	95	
67	36	93	
40	52	99	
61	52	83	

FIGURE 3.10. The beach ball of normal fault. The vertical velocity of the formation is used for velocity model. The second row is the theoretical strike, dip, rake, and beach ball of a normal fault. The third row represents moment tensor inversion of synthetic seismograms considering far-field terms and intermediate-field terms. The fourth row represents moment tensor inversion of synthetic seismograms considering only considering far-field terms. The fifth row represents moment tensor inversion of synthetic seismograms with 10% noise considering far-field terms and intermediate-field terms. The sixth row represents moment tensor inversion of synthetic seismograms with 10% only considering far-field terms.

the theoretical ones. Because the location errors of sources, the moment tensor inversion changes.

3.4 Conclusions

We use the inverse model in this chapter to get the moment tensor inversion from theoretical seismograms from different sources, double couple and CLVD sources. Homogenous and isotropic media and anisotropic media are also considered in the study to see if the results are improved by considering intermediate-field terms in analysis the source mechanism. The results indicate that intermediate-field terms

are helpful in the intermediate-field terms into the inversion algorithm to obtain the moment tensors. The intermediate-field terms can improve moment tensor inversion by 2% to 5% at the 1000ft source-receiver distance. When distance is longer than 6700 ft, the improvement is limited to less than 1%.

Noise is also added into the synthetic seismograms, because the geophones record a high amplitude of noise in real applications. The intermediate-field terms improves the moment tensor inversion more effectly when there is noise in isotropic medium (15% improvement with noise present vs 3% improvement without noise).

We also use the inversion method to get the source mechanism from synthetic seismograms in anisotropic medium. The intermediate-field terms can improve moment tensor inversion by 2% to 40% at the 1000 ft distance in homogeneous and anisotropic medium. When distance is longer than 6700 ft, the improvement is limited to 1%. The intermediate field terms also improves the moment tensor inversion when there is noise in anisotropic medium (20% improvement with noise vs 5% improvement without noise).

In all of the cases we considered above, the results of moment tensor inversion become more precise when including intermediate-field terms. The amplitudes of P wave and S wave increase in the synthetic seismograms and doing moment tensor inversion. Only relative amplitudes and polarities of first arrival of P wave and S wave changes with different sources. The amplitude of intermediate field terms is proportion to far-field terms. When the source-receiver distance is close enough (less than 1000 ft (300 m)), considering intermediate-field terms should increase the precision of moment tensor inversion.

Chapter 4

Summary, Conclusions and Recommendations

4.1 Summary of Research

We start our research about the microseismic events associated with hydraulic fracture propagation from a very simple model, due to the complexity of the problem due to heterogeneity, anisotropy, different and irregular layers. The method to study the source mechanism of microseismic events is based on earthquake study methodology. The method to study the source mechanism of microseismic events is based on earthquake study methodology. There are some differences between earthquakes and microseismic events: the distance between the source and receiver, the geometry of source and geophones, and the magnitude of earthquakes and microseismic events. Aki and Richards (2002) have pointed out that intermediate-field terms need to be considered for situations when the source is located less than 6700 ft (2000 m) from the receivers. In the case of microseismic events, the source-receiver distance is usually 1000 ft (300 m) to 2000 ft (600 m), which is close enough to consider intermediate-field terms.

A very simple model is used to study microseismic events: a homogenous isotropic elastic medium. The fracture is considered as a distribution of dislocations. I generate synthetic seismograms based on the displacement equation (Equ. 2.10) and verify them. Then, the fracture can be considered as a double couple, which represents a normal fault. We generate seismograms only using far-field terms and verify the adapted code with published results. In the next step, the seismograms incorporating intermediate-field terms are used to determine the source-receiver distance at which the intermediate-field terms cannot be ignored. The synthetic

seismograms from different DC and CLVD sources are also generated as well as noise in homogenous and isotropic media. Because the layers in formation are usually anisotropic, the synthetic seismograms (or with noise) from different DC and CLVD are both produced in homogenous and anisotropic media.

To study the effect of intermediate-field terms, we do moment tensor inversion by using the seismograms from a simple model. First, we do moment tensor inversion, considering only far-field terms or both far- and intermediate-field terms, from homogenous and isotropic media to get the double couple or CLVD sources. In the next, we considered noise is recorded by the geophones and get the beach ball. In the end we do it from homogenous and anisotropic media. From the output result, we can get the angels of the crack and the moment tensor, which represented by a matrix.

4.2 Conclusions

From all the results, we can conclude that:

- The intermediate-field term contributes 1/3 of the signal amplitude when the source-receiver distance is 1000ft (300 m) (Chapter 2 Section 2.2.3).
- The intermediate-field term contributes 1/20 of the signal amplitude when the source-receiver distance is 6700 ft (2000 m). Note that 1/20 is the noise level (Chapter 2 Section 2.2.4).
- Thus, when the source-receiver distance is less than 6700 ft (2000 m), we need to consider the intermediate-field term. Especially when the distance is than 1000ft (300 m), the intermediate-field term becomes significant (Chapter 2 Section 2.2.4).
- The near-field terms contribute less than 1/20 of the signal amplitude when the separation is more than 300 ft (100 m). Thus, in a general case, we con-

firmed that near-field term can be ignored in microseismic analysis (Chapter 2 Section 2.2.3).

- The intermediate-field terms can improve moment tensor inversion by 2% to 3% at the 1000 ft (300 m) separation in homogeneous and isotropic medium. When separation is greater than 6700 ft (2000 m), the improvement is limited to less than 1% (Chapter 3 Section 3.2.1).
- The intermediate-field terms improve the moment tensor inversion more significantly when there is noise in isotropic medium (15% improvement with noise present vs 3% improvement without noise) (Chapter 3 Section 3.2.2).
- The intermediate-field terms can improve moment tensor inversion by 2% to 40% for 1000 ft (300 m) separation in homogeneous and anisotropic medium. When separation is more than 6700 ft (2000 m), the improvement is limited to 1% (Chapter 3 Section 3.3). The intermediate field terms also improve the moment tensor inversion when there is noise in anisotropic medium (20% improvement with noise vs 5% improvement without noise) (Chapter 3 Section 3.3).

4.3 Recommendations

- Improve the method to do moment tensor inversion that mainly P and S wave to invert seismograms by considering the changing velocity into the algorithm used in this thesis. (Hydraulic fracturing is generated stage by stage. Each stage will cause the velocity change in the formation.)
- Improve the method to do moment tensor inversion that mainly using P and S wave to invert seismograms by considering the anisotropy effects into the algorithm used in this thesis. To considering the anisotropy effects, we

can use the internal code in Ray Tracing software FAST to get the synthetic seismograms in anisotropic media to get the synthetic seismograms. And then input the seismograms into the algorithm to do the inversion. The reason is that the anisotropy in microseismic events cannot be ignored.

- Apply the source mechanism methodology doing moment tensor inversion on real microseismic data from the field, ultimately help to estimate the geometry of the hydraulic fracture zone and certain dynamics of the fracturing process more precisely.

References

- [1] Adachi, J., Siebrits, E., Peircec, A., and J. Desroches, (2007). Computer simulation of hydraulic fractures. *International Journal of Rock Mechanics & Mining Sciences* 44, pages: 739 - 757.
- [2] Aki, K. and P. G. Richards, (1980). *Quantitative Seismology: Theory and Methods*, W. H. Freeman, New York.
- [3] Aki, K. and P. G. Richards, (2002). *Quantitative Seismology: Theory and Methods*, W. H. Freeman, New York.
- [4] Albright, J.N., and C.F. Pearson. (1982). Acoustic Emissions as a Tool for Hydraulic Fracture Location: Experience at the Fenton Hill Hot Dry Rock Site, August. <http://www.osti.gov/scitech/servlets/purl/6011566>.
- [5] Alkhalifah, T. (1998). An acoustic wave equation for orthorhombic anisotropy. *SEG* 263275.
- [6] Alkhalifah, T. (2000). An acoustic wave equation for anisotropic media. *SEG*, 03.
- [7] Backus, G. E. (1977). Interpreting the seismic glut moments of total degree two or less. *Geophys. J. R. Astr. Soc.* 51, 1-25.
- [8] Backus, G. E. and M. Mulcahy (1976). Moment tensors and other phenomenological descriptions of seismic sources. *Geophysics. J. R. Astr. Soc.* 46, 341-361.
- [9] Baig, A. and T. Urbancic, (2010). Microseismic moment tensors: a path to understanding frac growth. *The Leading Edge*.
- [10] Ben-Menahem, A and S. J. Singh, (2000). *Seismic Waves and Sources*.
- [11] Ben-Menahem, A., R. L. Gibson and A. G. Sena, (1991). Green's tensor and radiation patterns of point sources in general anisotropic inhomogeneous elastic media. *Geophys. J. Int.* (1991) 107 (2): 297-308.
- [12] Berumen, S., Tiab, D. and F. Rodriguez, (2000). Constant rate solutions for a fractured well with an asymmetric fracture. *Journal of Petroleum Science and Engineering*, 25, pages: 49-58.
- [13] Board, M., Rorke, T., Williams, G. and N. Gay, (1992). Fluid injection for rock burst control in deep mining. *Proceedings of the 33rd U.S. symposium on rock mechanics*. Rotterdam: Balkema, pages: 11120.

- [14] Boroumand, N., and H. Bland, (2012). Noise and its effect on microseismic event locations. GeoConvention. <http://www.cspg.org/documents/Conventions/Archives/Annual2012/286GC2012NoiseanditsEffectonMicroseismicEventLocations.pdf>
- [15] Bullen, K. E. and B. A. Bolt (1985). An introduction to the theory of Seismology. Cambridge University Press, Cambridge.
- [16] Calvez, J.H. L., et al., (2007). Real-time Microseismic monitoring of hydraulic fracture treatment: A tool to improve completion and reservoir management. SPE 106159.
- [17] Cipolla, C.L. and Wright, C.A., (2000). Diagnostic Techniques to Understand Hydraulic Fracturing: What? Why? and How? SPE 59735 presented at the SPE/CERI Gas Technology Symposium, Calgary, 35 April.
- [18] Dahm, T. (1996). Relative moment tensor inversion based on ray theory: theory and synthetic tests. *Geophysical Journal International*, 124(1), 245-257.
- [19] Drader, D., et al., (2012). Improved Power Production Efficiency of Hydrothermal Reservoirs Using Downhole Pumps. Stanford Geothermal Workshop.
- [20] Du, J., and N. R. Warpinski, (2013). Velocity Building for Microseismic Hydraulic Fracture Mapping in Isotropic and Anisotropic Media. SPE 163866.
- [21] Du, J., and N. Warpinski, (2011). Uncertainty in Fault Plane Solutions from Moment Tensor Inversion due to Uncertainty in, *SEG*, 1(4), 1534-1538.
- [22] Dziewonski, A. M. and J. H. Woodhouse. (1983). Studies of the seismic sources using normal-mode theory. *Earthquakes: Observation, Theory and Interpretation*.
- [23] Eaton, D. W. (2009). Resolution of microseismic moment tensors: A synthetic modeling study. *SEG*, 3569-3574.
- [24] Economides, M. J., and K. G. Nolte, (2008). *Reservoir stimulation*. ISBN-10: 0471491926.
- [25] Environmental Protection Agency, (2012). <http://www2.epa.gov/hfstudy/hydraulic-fracturing-water-cycle>
- [26] Fagan, D., K. Van Wijk, and J. Rutledge, (2013). Clustering revisited?: A spectral analysis of microseismic events. *Geophysics*, 78(2).
- [27] Friedrich, A., F. Kruger, and K. Klinge, (1998). Ocean-generated microseismic noise located with the Grafenberg array. *Journal of Seismology*, 4764.

- [28] Geller, R. J. (1976). Body force equivalents for stress-drop seismic sources, *Bull. Seism. Soc. Am.* 66, 1801-1804.
- [29] Gilbert, F. (1970). Excitation of the normal modes of the earth by earthquakes sources, *Geophys. J. R. Astr. Soc.*
- [30] Gilbert, F. and A. M. Dziewonski. (1975). An application of normal mode theory to the retrieval of structural parameters and source mechanisms from seismic spectra. *Phil. Trans. R. Soc. A* 278, 187-269.
- [31] Grebe, J.J. and Stoesser, M., (1935). Increasing crude production 20,000,000 bbl. from established fields, *World Petroleum J.*, (August), pages: 47382.
- [32] Hainey, B.W., R.G. Keck, M.B. Smith, K.W. Lynch, and J.W. Barth, (1999). On-site fracturing disposal of oilfield-waste solids in Wilmington field, California. *SPE PRODUCTION & FACILITIES*, Volume 14, pages: 88-93.
- [33] Haskell, N. A. (1964). Total energy and energy spectral density of elastic wave radiation from propagating faults. *Bull. Seism. Soc. Am.* 54, 1811-1841.
- [34] Hayashi, K., A. Sato, and T. Ito, (1997). In situ stress measurements by hydraulic fracturing for a rock mass with many planes of weakness. *International Journal of Rock Mechanics & Mining Sciences*, 34, pages: 45-58.
- [35] Honda, H. (1962). Earthquake mechanism and seismic waves, *Geophysical Notes*, *Geophys. Inst., Fac. of Science, Tokyo Univ.* 15, 1-97.
- [36] Hons, M., Stewart, R., Lawton, D., and Bertram, M., (2007). Ground Motion Through Geophones And MEMS Accelerometers: Sensor Comparison In Theory, Modeling and Field Data, paper 2007-0011 presented at SEG Annual Meeting, San Antonio, Texas
- [37] Hons, M., et al., (2008). Acoustic and optical borehole-wall imaging for fractured-rock aquifer studies Accelerometer vs Geophone Response: A Field Case History. CSPG.
- [38] House, L. S. (1987). Locating microearthquakes induced by hydraulic fracturing in crystalline rock, *Geophys. Res. Lett.*, 14, 919-921.
- [39] Hunt, J.L., K. Frazier, Pendergraft, B.P. and Soliman, M.Y., (1994). Evaluation and 13 completion procedures for produced brine and waste-water disposal wells. *Journal of Petroleum Science and Engineering*, 11, pages: 51-60.
- [40] Ichinose, G. A., Peter Goldstein and Arthur J. Rodgers, (2000) Relative importance of near-, intermediate- and far-field displacement terms in layered earth synthetic seismograms. *Bulletin of the Seismological Society of America*, 90(2):531-536.

- [41] Jahnke, G. (2004). Free open source MATLAB code anaseis.m. [http://www.quest-itn.org/library/software/understanding seismic radiation patterns tutorial](http://www.quest-itn.org/library/software/understanding%20seismic%20radiation%20patterns%20tutorial)
- [42] Julian, B. R., A. D. Miller, and G. R. Foulger (1998), Non-double-couple earthquakes 1. Theory, *Rev. Geophys.*, 36(4), 525-549, doi:10.1029/98RG00716.
- [43] Jost, M.L. and R.B. Herrman, (1989). A students guide to and review of moment tensors, *Seism. Res. Letters*, 60, 37-57.
- [44] Kanamori, H. (1995). Moment-Tensor Inversions for Local Earthquakes Using Surface Waves Recorded at TERRAScope, *Bulletin of the Seismological Society of America*, 85(4), 1021-1038.
- [45] Kanamori, H. and J. W. Given, (1981). Use of long-period surface waves for rapid determination of earthquake-source parameters. *Phys. Earth Planet.*
- [46] Kawakatsu, H. (1989). Centroid single force inversion of seismic waves generated by landslides. *J. Geophys. Res.* 94, 12363-12374.
- [47] Kikuchi, M., and H. Kanamori, (1982). Inversion of complex body waves, *Bulletin of the Seismological Society of America*, 72(2), 491-506.
- [48] Knill, J.L., J.A. Franklin, A.W. Malone, A study of acoustic emission from stressed rock, *International Journal of Rock Mechanics and Mining Sciences and Geomechanics Abstracts*, Volume 5, Issue 1, January 1968, Pages 87-88, ISSN 0148-9062, [http://dx.doi.org/10.1016/0148-9062\(68\)90025-9](http://dx.doi.org/10.1016/0148-9062(68)90025-9).
- [49] Kostrov, B. V. and S. Das, (1988). *Principles of earthquake source mechanics*. Cambridge University Press.
- [50] Lee, W. et al., (2002). *International Handbook of Earthquake and Engineering*, Academic Press.
- [51] Lokmer, I., and Christopher J. Bean, (2010). Properties of the near-field term and its effect on polarisation analysis and source locations of long-period (LP) and very-long-period (VLP) seismic events at volcanoes, *Journal of Volcanology and Geothermal Research*, Volume 192, Issues 12, 20 April 2010, Pages 35-47, ISSN 0377-0273, <http://dx.doi.org/10.1016/j.jvolgeores.2010.02.008>.
- [52] Madariaga, R., (2007). Seismic source theory, Chapter 2 of vol 4, *Earthquake seismology* H. Kanamori ed., *Treatise of Geophysics*, Academic Press.
- [53] Martins, P.J. et al. (1992). Deviated Well Fracturing and Proppant Production Control in the Prudhoe Bay Field. paper SPE 24858 presented at the 1992 SPE Annual Technical Conference and Exhibition, Washington, Oct. 4-7.

- [54] Mavko, G. et al., (1998). The Rock Physics Handbook, Cambridge University Press.
- [55] Maxwell, S. C., Urbancic, T. I., Steinsberger, N., Energy, D., and Zinno, R. (2002). Microseismic Imaging of Hydraulic Fracture Complexity in the Barnett Shale. SPE 77440.
- [56] McCowan, D. W. (1976). Moment tensor representation of surface wave sources, Geophys. J. R. Astr. Soc. 44, 595-599.
- [57] McDaniel, B.W., E. Marshall, L. East, and J. Surjaatmadja Tester, Jefferson, Robert Bivins, and Robert Potter. (1982). Interwell tracer analyses of a hydraulically fractured granitic geothermal reservoir. Old SPE Journal 22.4 (1982): 537-554.
- [58] Mendiguren, J. A. (1977). Inversion of surface wave data in source mechanism studies, J. Geophys. Res. 82, 889-894
- [59] Miller, Brent et al., (2008). The successful application of a compartmental completion technique used to locate multiple hydraulic-fracture treatments in horizontal Bakken Shale wells in North Dakota, SPE 116469.
- [60] Murdoch, L. C., and W. W. Slack, (2002). Forms of hydraulic fractures in shallow fine grained formations. Journal of Geotechnical and Geoenvironmental Engineering, 128, pages: 479-487.
- [61] Nettles, M., and G. Ekstrom (1998), Faulting mechanism of anomalous earthquakes near Brdarbunga Volcano, Iceland, J. Geophys. Res., 103(B8), 1797317983, doi:10.1029/98JB01392
- [62] Northrop, D. A. and K. H. Frohne, (1990), the multiwell experiment A field laboratory in tight gas sandstone reservoirs. JPT
- [63] Paillet, F. L. (1998), Flow modeling and permeability estimation using borehole flow logs in heterogeneous fractured formations, Water Resour. Res., 34(5), 9971010, doi:10.1029/98WR00268.
- [64] Potter, Robert M., (1977). Hydraulic Fracture Initiation Sites in Open Boreholes Identified by Geophysical Logs. No. SGP-TR-25-6. University of California, Los Alamos National Laboratory (LANL), Los Alamos, NM.
- [65] Raaen, A.M., Skomedal, E., Kjørholt, H., Markestad, P. and Okland, D., (2001). Stress determination from hydraulic fracturing tests: The system stiffness approach. International Journal of Rock Mechanics and Mining Sciences, 38, pages: 529-541.
- [66] Rabim, Zillur et al., (2012). Productivity increase using hydraulic fracturing in conventional and tight gas reservoirs expectation vs. reality, Saudi Aramco Journal of Technology.

- [67] Rietsch, E., (2000). Open source MATLAB package: SeisLab. [http://www.mathworks.com/matlabcentral/fileexchange/15674](http://www.mathworks.com/matlabcentral/fileexchange/15674_seislab) seislab 3 01
- [68] Romanowicz, B. and T. Monfret, (1986). Source process times and depths of large earthquakes by moment tensor inversion of mantle wave data and the effect of lateral heterogeneity. *Ann. Geophys.* 4, 271-183.
- [69] Rosen, R.L., (1994). Antrim Shale Hydraulic Fracture Diagnostics, presented at the joint GRIrSoc. Petr. Eng. Advances in Antrim Shale Technology Workshop, Mt. Pleasant, MI.
- [70] Sasaki, S., (1998). Characteristics of microseismic events induced during hydraulic fracturing experiments at the Hijiori hot dry rock geothermal energy site, Yamagata, Japan. *Tectonophysics*, 289, pages: 171-188.
- [71] Shuler, A. et al., (2013). Physical mechanisms for vertical-CLVD earthquakes at active volcanoes, *Journal of Geophysical Research: Solid Earth*.
- [72] Sokos, E. N., and Zahradnik, J. (2008). ISOLA a Fortran code and a Matlab GUI to perform multiple-point source inversion of seismic data. *Computers & Geosciences*, 34(8), 967 - 977.
- [73] Stump, B. W. and L. R. Johnson. (1977). The determination of source properties by the linear inversion of seismograms. *Bull. Seism. Soc. Am.* 67, 1489-1502.
- [74] Thomsen, L. (1986). Weak elastic anisotropy. *GEOPHYSICS*, 51(10), 1954-1966. doi: 10.1190/1.1442051
- [75] Urbancic, T.I., Shumila, V., Rutledge, J.T., and Zinno, R. (1999). Determining hydraulic fracture behavior using microseismicity. *Rock Mechanics for USRM Mtg, Industry, Ann.*
- [76] Veatch, R.W., Moschovidis, Z.A., Fast, C.R., (1989). An overview of hydraulic fracturing. In: Gidley, Holditch, Nierode, Veatch, editors. *Recent advances in hydraulic fracturing. Monograph, Vol. 12*, Richardson: Society of Petroleum Engineers, p. 138.
- [77] Valkó, P. and M.J. Economides, (1995). *Hydraulic Fracture Mechanics*, Wiley.
- [78] Vavryčuk, V. (2001). Inversion for parameters of tensile earthquakes. *J. of Geophysical Research*, 106 (B8): 16339-16355.
- [79] Vavryčuk, V. (2007). On the retrieval of moment tensors from borehole data. *Geophysical Prospecting*, 55 (3): 381-391.

- [80] Ward, S. N. (1980). Body wave calculations using moment tensor sources in spherically symmetric inhomogeneous media. *Geophys. J. R. Astr. Soc.* 60, 53-66.
- [81] Warpinski, N. R. et al., (2001). Analysis and prediction of microseismicity induced by hydraulic fracturing: SPE 71649.
- [82] Warpinski, N.R., et al., (1995). Microseismic Mapping of Hydraulic Fractures Using Multi-Level Wireline Receivers. SPE Annual Technical Conference and Exhibition, 579589.
- [83] Warpinski, N. R., C. K. Waltman, J. Du, (2009). Anisotropy Effects in Microseismic Monitoring, SPE 124208 0(October), 47.
- [84] Warpinski, N., and J. Du, (2010). Source-Mechanism Studies on Microseismicity Induced by Hydraulic Fracturing. Proceedings of SPE Annual Technical Conference and Exhibition.
- [85] Warpinski, N. R., and J. C. Lorenz, (2008), Analysis of the multiwell experiment data and results: Implications for the basin-centered gas model, in S. P. Cumella, K. W. Shanley, and W. K. Camp, eds., Understanding, exploring, and developing tight-gas sands 2005 Vail Hedberg Conference: AAPG Hedberg Series, no. 3, p. 157-176.
- [86] Warpinski, N. R., Branagan, P. T., Peterson, R. E., Fix, J. E., Uhl, J. E., Engler, B. P., and Wilmer, R. (1997, January 1). Microseismic and Deformation Imaging of Hydraulic Fracture Growth and Geometry in the C Sand Interval, GRI/DOE M-Site Project. Society of Petroleum Engineers. doi:10.2118/38573-MS
- [87] Warpinski, N.R. (1991). Hydraulic Fracturing in Tight, Fissured Media, February. <http://www.osti.gov/scitech/servlets/purl/6023906>.
- [88] Warpinski, N. R., Branagan, P. T., Peterson, R. E., Wolhart, S. L., and Uhl, J. E. (1998, January 1). Mapping Hydraulic Fracture Growth and Geometry Using Microseismic Events Detected by a Wireline Retrievable Accelerometer Array. Society of Petroleum Engineers. doi:10.2118/40014-MS
- [89] Warpinski, N.R., B.P. Engler, C.J. Young, R. Peterson, P.T. Branagan, and J.E. Fix. (1995). Microseismic Mapping of Hydraulic Fractures Using Multi-Level Wireline Receivers. SPE Annual Technical Conference and Exhibition, 579589.
- [90] Wright, C. A., et al., (1998). Downhole tiltmeter fracture mapping: Finally measuring hydraulic fracture dimensions. SPE 46194.
- [91] Wright, C. A., et al., (1999). Downhole tiltmeter fracture mapping: A new tool for direct measurement of hydraulic fracture growth. Rock Mechanics Symposium.

- [92] Williams, J. H., and Carole D. Johnson, (2004). Acoustic and optical borehole-wall imaging for fractured-rock aquifer studies, *Journal of Applied Geophysics*, Volume 55, Issues 12, January 2004, Pages 151-159, ISSN 0926-9851, <http://dx.doi.org/10.1016/j.jappgeo.2003.06.009>. (<http://www.sciencedirect.com/science/article/pii/S0926985103000764>)
- [93] Williams-stroud, S., and R. L Billingsley,, (2010). Techniques to estimate fracture effectiveness when mapping low-magnitude microseismicity mapping fractures from low-magnitude microseismicity. SEG, 20752079.
- [94] Willson, D. J., et al., (1993). Cleanup of fractured rock aquifers: Implications of matrix diffusion. *Environmental Monitoring and Assessment* January 1993, Volume 24, Issue 1, pp 45-70
- [95] Young, R. P. (1992). Moment Tensor Inversion of Induced Microseismic Events: Evidence Of Non-Shear Failures In The $-4 < M < -2$ Moment Magnitude Range. *Geophysical Search Letters*.
- [96] Zimmer, U., Maxwell, S. C., Waltman, C. K., and Warpinski, N. R. (2009, December 1). Microseismic Monitoring Quality-Control (QC) Reports as an Interpretative Tool for Nonspecialists. Society of Petroleum Engineers. doi:10.2118/110517-PA
- [97] Zimmer, U. (2010). Localization of microseismic events Using head waves and direct waves. SEG.

Appendix A: Synthetic Seismogram Calculation

To generate the synthetic seismograms for moment tensors, MATLAB programs are needed.

TABLE A.1: The MATLAB programs for seismograms generated by a moment tensor

Program	Function
Ricker.m	Generate a single Ricker wavelet
Dtricker.m	A time derivative of a single Ricker wavelet
Dttricker.m	A second time derivative of a single Ricker wavelet
Nricker.m	The time integral of a single Ricker wavelet
Ntricker.m	A derivative of time times the time integral of a single Ricker wavelet
geophoneCoords.m	The geophone coordinates in Cartesian Coordinates
dipoleDC.m	Calculate the synthetic seismogram for isotropic medium the input parameters are density (kg/m^3), Young's Modulus (Pa), Poisson's ratio, Start time (s), End time (s), time interval (s), the dominant frequency of Ricker wavelet(Hz), the location of the source in Cartesian Coordinates (m), the type of the source (3 by 3 matrix)
plotseismogram.m	Plot the seismograms with all terms, far-field terms, intermediate-field terms, and near-field terms, save one type of the seismograms in different .dat file
Continued on next page	

Table A.1 – continued from previous page

Program	Function
dipoleDC11.m	Calculate the synthetic seismogram for isotropic medium the input parameters are density (kg/m^3), P wave velocity (km/s), S wave velocity (km/s), Start time (s), End time (s), time interval (s), the dominant frequency of Ricker wavelet(Hz), the location of the source in Cartesian Coordinates (m), the type of the source (3 by 3 matrix)
dipoleDCnoisev.m	Calculate the synthetic seismogram with noise the input parameters are density (kg/m^3), Young's Modulus (Pa), Poisson's ratio, Start time (s), End time (s), time interval (s), the dominant frequency of Ricker wavelet(Hz), the location of the source in Cartesian Coordinates (m), the frequency of noise (Hz) and SNR
dipoleDCiso.m	Calculate the synthetic seismogram for anisotropic medium the input parameters are density (kg/m^3), vertical P wave velocity (km/s), vertical S wave velocity (km/s), horizontal P wave velocity (km/s), horizontal S wave velocity (km/s), Start time (s), End time (s), time interval (s), the dominant frequency of Ricker wavelet(Hz),
Continued on next page	

Table A.1 – continued from previous page

Program	Function
	<p>the location of the source in Cartesian Coordinates (m),</p> <p>the type of the source (3 by 3 matrix)</p> <p>the displacement and velocity are calculate separately</p>
dipoleDCisonoi.m	<p>Calculate the synthetic seismogram for anisotropic medium</p> <p>The noise is exist in the synthetic seismograms</p> <p>the input parameters are density (kg/m^3),</p> <p>vertical P wave velocity (km/s),</p> <p>vertical S wave velocity (km/s),</p> <p>horizontal P wave velocity (km/s),</p> <p>horizontal S wave velocity (km/s),</p> <p>Start time (s), End time (s), time interval (s),</p> <p>the dominant frequency of Ricker wavelet(Hz),</p> <p>the frequency of noise (Hz) and SNR</p> <p>the location of the source in Cartesian Coordinates (m),</p> <p>the type of the source (3 by 3 matrix)</p> <p>the displacement are calculate from the integral of velocity</p>

```
function dipoleDC()
```

```
clear all;
```

```
clc;
```

```
close all;
```

```
icheck = 1;
```



```

tic

%-----

density = 2.0*1000; %Density in ,use SS property from 2.09 to 2.67

E = 30*10000000000; %Young's Modulus in GPa, from 3.24 to 99.9GPa

poission=0.3; %Poisson's ratio, from 0.2 to 0.35

t1 = 0.00; % Starting time

t2 = 0.2; % end time

deltat = 0.0001; %Time step

Xsource = [0.0D0; 0.0D0; 0.0D0];

%----- Source information -----

% choose a source type:

% 1 is the impluse can be seen as a sin function

% 2 is ricker wavelet

type=2; % 1 or 2

if type==2

f0=100; %frequency in ricker wavelet

elseif type==1

as=100000.00; %Amplitude of sin function

bs=10.00*pi; %frenquency of sin function

else error('not a correct type (sorry)')

end

%-----

% Time

Ndt = (t2-t1)/deltat+1; % Number of time-interval

Ndt1 = floor (Ndt);

t(:,1) = t1: deltat : t2; % Seismogram time

```

```

fprintf(' Number of time intervals: %.0f ', Ndt)

% -----

% Elastic properties

lambda = E*possion/((1+possion)*(1-2*possion)); % Lamé's constant
mu = E/(2.0*(1.0+possion)); % Lamé's Const.

alpha = ( (lambda+2.0*mu)/density)0.50; % const relate to P-wave in wave
equation

beta = (mu/density)0.50; % const relate to S-wave in wave equation

% -----

% Geophones

x = geophoneCoords();

gnum = size(x,1); % Number of Geophones

reciu = zeros(gnum, 3, Ndt1); %total displacement
reciv = zeros(gnum, 3, Ndt1); %total velocity
reciun = zeros(gnum, 3, Ndt1); %displacement caused by near-field term
recivn = zeros(gnum, 3, Ndt1); %velocity caused by near-field term
reciui = zeros(gnum, 3, Ndt1); %displacement caused by intermediate-field term
recivi = zeros(gnum, 3, Ndt1); %velocity caused by intermediate-field term
reciuf = zeros(gnum, 3, Ndt1); %displacement caused by far-field term
recivf = zeros(gnum, 3, Ndt1); %velocity caused by far-field term

i=1:gnum;

r(i,1)=sqrt((x(i,3)-Xsource(3)).2+(x(i,2)-Xsource(2)).2+(x(i,1) ... -Xsource(1)).2);

% Distance from zero to geophone

% -----

% Coordinate Transformation

vr = zeros(gnum, 3);

```

```

vphi= zeros(gnum, 3);
vtheta=zeros(gnum, 3);
theta= acos((x(i, 3)-Xsource(1))./r(i));
phi = atan2((x(i,1)-Xsource(1)),(x(i,2)-Xsource(2)))-pi/2;
if icheck == 1
fprintf(' Geophones in spherical coordinate system ')
for j =1:gnum
fprintf(' r = %.3f Theta = %.3f P̂hi= %.3f ',r(j),theta(j),phi(j))
end
end
%----- coordinate transform -----
vr(i, 1) = cos(phi(:)).*sin(theta(:));
vr(i, 2) = sin(phi(:)).*sin(theta(:));
vr(i, 3) = cos(theta(:));
vphi(i, 1) = -1.*sin(phi(:));
vphi(i, 2) = cos(phi(:));
vphi(i, 3) = 0.00;
vtheta(i, 1) = cos(phi(:)).*cos(theta(:));
vtheta(i, 2) = sin(phi(:)).*cos(theta(:));
vtheta(i, 3) = -1.*sin(theta(:));
%----- Constants -----
Const1 = 1./(4*pi*density*alpha2)./r.2; %Const for intermediate-field P-wave
term in Eq.4.32 Aki
Const2 = 1./(4*pi*density* beta2)./r.2; %Const for intermediate-field S-wave
term in Eq.4.32 Aki
Const3 = Const1/alpha.*r; %Const for far-field P-wave term in Eq.4.32 Aki

```

```

Const4 = Const2/beta.*r; %Const for far-field S-wave term in Eq.4.32 Aki
Const5 = 1./(4*pi*density)./r.4; %Const for near-field wave term in Eq.4.32 Aki
fprintf(' - Time before radiation pattern calulation %.2f ', toc)

% ————— Radiation Patterns —————

An(i,1:3) = (9*sin(2*theta).*cos(phi))*ones(1,3).*vr(i,1:3)...
-(6*cos(2*theta).*cos(phi))*ones(1,3).*vtheta(i,1:3) ...
+(6*cos(theta).*sin(phi))*ones(1,3).*vphi(i,:); %near-field
Aip(i,:) = 4*sin(2*theta).*cos(phi)*ones(1,3).*vr(i,:) ...
-2*(cos(2*theta)).*cos(phi)*ones(1,3).*vtheta(i,:) ...
+2*cos(theta).*sin(phi)*ones(1,3).*vphi(i,:); % intermediate-field P-wave
Ais(i,:) = -3*sin(2*theta).*cos(phi)*ones(1,3).*vr(i,:) ...
+3*cos(2*theta).*cos(phi)*ones(1,3).*vtheta(i,:) ...
-3*cos(theta).*sin(phi)*ones(1,3).*vphi(i,:); % intermediate-field S-wave
Afp(i,:) = sin(2*theta).*cos(phi)*ones(1,3).*vr(i,:); %far-field P-wave
Afs(i,:) = cos(2*theta).*cos(phi)*ones(1,3).*vtheta(i,:) ...
-cos(theta).*sin(phi)*ones(1,3).*vphi(i,:); %far-field S-wave

%—————

if type==1
for m=1:gnum
for j=1:Ndt1
M0p1(j, m) = Impl(t(j)-r(m)/alpha,as,bs);
M0s1(j, m) = Impl(t(j)-r(m)/beta,as,bs);
M0pt1(j, m) = dtimpl(t(j)-r(m)/alpha,as,bs);
M0st1(j, m) = dtimpl(t(j)-r(m)/beta,as,bs);
M0ptt1(j, m) = dttimpl(t(j)-r(m)/alpha,as,bs);
M0stt1(j, m) = dttimpl(t(j)-r(m)/beta,as,bs);

```

```

NM01(j, m) = Nimpl(t(j)-r(m)/beta,as,bs,r(m)/beta)-Nimpl(t(j)-r(m)/
alpha,as,bs,r(m)/alpha);
NM0t1(j, m) = Ntimpl(t(j)-r(m)/beta,as,bs,r(m)/beta)-Ntimpl(t(j)-r(m)/
alpha,as,bs,r(m)/alpha);
end
end
elseif type==2
for j=1:gnum
ricker=Ricker(t-r(j)/alpha,f0);
M0p1(:, j)=ricker;
M0s1(:, j)=Ricker(t-r(j)/beta,f0);
M0pt1(:,j)=Dtricker(t-r(j)/alpha,f0);
M0st1(:,j)=Dtricker(t-r(j)/beta,f0);
M0ptt1(:,j)=Dttricker(t-r(j)/alpha,f0);
M0stt1(:,j)=Dttricker(t-r(j)/beta,f0);
NM01(:,j)=Nricker(t-r(j)/beta,f0,t)-Nricker(t-r(j)/alpha,f0,t);
NM0t1(:,j)=Ntricker(t,f0,r(j)/beta)-Ntricker(t,f0,r(j)/alpha);
end
end
% ----- Double Couple Matrix to calculate -----
for m=1:gnum
for j=1:Ndt1
% -----
% single dipole
% moment tensor -2, 0, 0; 0, 0, 0; 0, 0, 0;
M0p=[-2*M0p1(j, m), 0, 0; ... 0, 0*M0p1(j, m), 0; ... 0, 0, 0*M0p1(j, m)];

```

```

M0s=[-2*M0s1(j, m), 0, 0; ... 0, 0*M0s1(j, m), 0; ... 0, 0, 0*M0s1(j, m)];
M0pt=[-2*M0pt1(j, m), 0, 0; ... 0, 0*M0pt1(j, m), 0; ... 0, 0, 0*M0pt1(j, m)];
M0st=[-2*M0st1(j, m), 0, 0; ... 0, 0*M0st1(j, m), 0; ... 0, 0, 0*M0st1(j, m)];
M0ptt=[-2*M0ptt1(j, m), 0, 0; ... 0, 0*M0ptt1(j, m), 0; ... 0, 0, 0*M0ptt1(j, m)];
M0stt=[-2*M0stt1(j, m), 0, 0; ... 0, 0*M0stt1(j, m), 0; ... 0, 0, 0*M0stt1(j, m)];
NM0 = [-2*NM01(j, m), 0.00, 0.00;... 0.00, 0*NM01(j, m), 0.00;... 0.00, 0.00,
0*NM01(j, m)];

NM0t = [-2*NM0t1(j, m),0.00, 0.00;... 0.00, 0*NM0t1(j, m), 0.00;... 0.00,0.00,
0*NM0t1(j, m)];

%-----

% data4: vertical strike slip fault
% moment tensor 0, 0, 1; 0, 0, 0; 1, 0, 0;
M0p=[0, 0, 1*M0p1(j, m); ... 0, 0*M0p1(j, m), 0; ... 1*M0p1(j, m), 0, 0];
M0s=[0, 0, 1*M0s1(j, m); ... 0, 0*M0s1(j, m), 0; ... 1*M0s1(j, m), 0, 0];
M0pt=[0, 0, 1*M0pt1(j, m); ... 0, 0*M0pt1(j, m), 0; ... 1*M0pt1(j, m), 0, 0];
M0st=[0, 0, 1*M0st1(j, m); ... 0, 0*M0st1(j, m), 0; ... 1*M0st1(j, m), 0, 0];
M0ptt=[0, 0, 1*M0ptt1(j, m); ... 0, 0*M0ptt1(j, m), 0; ... 1*M0ptt1(j, m), 0, 0];
M0stt=[0, 0, 1*M0stt1(j, m); ... 0, 0*M0stt1(j, m), 0; ... 1*M0stt1(j, m), 0, 0];
NM0=[0, 0, 1*NM01(j, m); ... 0, 0*NM01(j, m), 0; ... 1*NM01(j, m), 0, 0];
NM0t=[0, 0, 1*NM0t1(j, m); ... 0,0*NM0t1(j, m) , 0; ... 1*NM0t1(j, m), 0, 0];

%-----

% data1 vertical strike slip fault
% moment tensor: 0, 1, 0; 1, 0, 0; 0, 0, 0;
M0p=[0, 1*M0p1(j, m),0; ... 1*M0p1(j, m),0, 0; ... 0*M0p1(j, m), 0, 0];
M0s=[0, 1*M0s1(j, m),0; ... 1*M0s1(j, m),0, 0; ... 0*M0s1(j, m), 0, 0];
M0pt=[0, 1*M0pt1(j, m), 0; ... 1*M0pt1(j, m), 0, 0 ; ... 0*M0pt1(j, m), 0, 0];

```

```

M0st=[0, 1*M0st1(j, m),0; ... 1*M0st1(j, m),0, 0; ... 0*M0st1(j, m), 0, 0];
M0ptt=[0, 1*M0ptt1(j, m),0; ... 1*M0ptt1(j, m), 0, 0; ... 0*M0ptt1(j, m), 0, 0];
M0stt=[0, 1*M0stt1(j, m),0; ... 1*M0stt1(j, m), 0, 0; ... 0*M0stt1(j, m), 0, 0];
NM0=[0, 1*NM01(j, m), 0; ... 1*NM01(j, m), 0, 0; ... 0*NM01(j, m), 0, 0];
NM0t=[0, 1*NM0t1(j, m),0; ... 1*NM0t1(j, m) ,0, 0; ... 0*NM0t1(j, m), 0, 0];
%----- % data 3 vertical dip
slip fault

% moment tensor: 0, 0, 0; 0, 0, 1; 0, 1, 0;

M0p=[0*M0p1(j, m), 0*M0p1(j, m), 0*M0p1(j, m); ... 0*M0p1(j, m), 0*M0p1(j,
m), 1*M0p1(j, m); ... 0*M0p1(j, m), 1*M0p1(j, m), 0*M0p1(j, m)];
M0s=[0*M0s1(j, m), 0*M0s1(j, m), 0*M0s1(j, m); ... 0*M0s1(j, m), 0*M0s1(j,
m), 1*M0s1(j, m); ... 0*M0s1(j, m), 1*M0s1(j, m), 0*M0s1(j, m)];
M0pt=[0*M0pt1(j, m), 0*M0pt1(j, m), 0*M0pt1(j, m); ... 0*M0pt1(j, m), 0*M0pt1(j,
m), 1*M0pt1(j, m); ... 0*M0pt1(j, m), 1*M0pt1(j, m), 0*M0pt1(j, m)];
M0st=[0*M0st1(j, m), 0*M0st1(j, m), 0*M0st1(j, m); ... 0*M0st1(j, m), 0*M0st1(j,
m), 1*M0st1(j, m); ... 0*M0st1(j, m), 1*M0st1(j, m), 0*M0st1(j, m)];
M0ptt=[0*M0ptt1(j, m), 0*M0ptt1(j, m), 0*M0ptt1(j, m); ... 0*M0ptt1(j, m),
0*M0ptt1(j, m), 1*M0ptt1(j, m); ... 0*M0ptt1(j, m), 1*M0ptt1(j, m), 0*M0ptt1(j,
m)];
M0stt=[0*M0stt1(j, m), 0*M0stt1(j, m), 0*M0stt1(j, m); ... 0*M0stt1(j, m),
0*M0stt1(j, m), 1*M0stt1(j, m); ... 0*M0stt1(j, m), 1*M0stt1(j, m), 0*M0stt1(j,
m)];
NM0=[0*NM01(j, m), 0*NM01(j, m), 0*NM01(j, m); ... 0*NM01(j, m), 0*NM01(j,
m), 1*NM01(j, m); ... 0*NM01(j, m), 1*NM01(j, m), 0*NM01(j, m)];

```

```

NM0t=[0*NM0t1(j, m), 0*NM0t1(j, m), 0*NM0t1(j, m); ... 0*NM0t1(j, m),
0*NM0t1(j, m) , 1*NM0t1(j, m); ... 0*NM0t1(j, m), 1*NM0t1(j, m), 0*NM0t1(j,
m)];

%-----

% double couple

%moment tensor: 0, 0, 1; 0, 0, 1; 1, 1, 0;

M0p=[0*M0p1(j, m), 0*M0p1(j, m), 1*M0p1(j, m); ... 0*M0p1(j, m), 0*M0p1(j,
m), 1*M0p1(j, m); ... 1*M0p1(j, m), 1*M0p1(j, m), 0*M0p1(j, m)];

M0s=[0*M0s1(j, m), 0*M0s1(j, m), 1*M0s1(j, m); ... 0*M0s1(j, m), 0*M0s1(j,
m), 1*M0s1(j, m); ... 1*M0s1(j, m), 1*M0s1(j, m), 0*M0s1(j, m)];

M0pt=[0*M0pt1(j, m), 0*M0pt1(j, m), 1*M0pt1(j, m); ... 0*M0pt1(j, m), 0*M0pt1(j,
m), 1*M0pt1(j, m); ... 1*M0pt1(j, m), 1*M0pt1(j, m), 0*M0pt1(j, m)];

M0st=[0*M0st1(j, m), 0*M0st1(j, m), 1*M0st1(j, m); ... 0*M0st1(j, m), 0*M0st1(j,
m), 1*M0st1(j, m); ... 1*M0st1(j, m), 1*M0st1(j, m), 0*M0st1(j, m)];

M0ptt=[0*M0ptt1(j, m), 0*M0ptt1(j, m), 1*M0ptt1(j, m); ... 0*M0ptt1(j, m),
0*M0ptt1(j, m), 1*M0ptt1(j, m); ... 1*M0ptt1(j, m), 1*M0ptt1(j, m), 0*M0ptt1(j,
m)];

M0stt=[0*M0stt1(j, m), 0*M0stt1(j, m), 1*M0stt1(j, m); ... 0*M0stt1(j, m),
0*M0stt1(j, m), 1*M0stt1(j, m); ... 1*M0stt1(j, m), 1*M0stt1(j, m), 0*M0stt1(j,
m)];

NM0=[0*NM01(j, m), 0*NM01(j, m), 1*NM01(j, m); ... 0*NM01(j, m), 0*NM01(j,
m), 1*NM01(j, m); ... 1*NM01(j, m), 1*NM01(j, m), 0*NM01(j, m)];

NM0t=[0*NM0t1(j, m), 0*NM0t1(j, m), 1*NM0t1(j, m); ... 0*NM0t1(j, m),
0*NM0t1(j, m) , 1*NM0t1(j, m); ... 1*NM0t1(j, m), 1*NM0t1(j, m), 0*NM0t1(j,
m)]; %-----

%----- CLVD

```



```

% moment tensor: 1, 0, 0; 0, -2, 0; 0, 0, 1;

M0p=[1*M0p1(j, m), 0*M0p1(j, m), 0*M0p1(j, m); ... 0*M0p1(j, m), -2*M0p1(j,
m), 0*M0p1(j, m); ... 0*M0p1(j, m), 0*M0p1(j, m), 1*M0p1(j, m)];

M0s=[1*M0s1(j, m), 0*M0s1(j, m), 0*M0s1(j, m); ... 0*M0s1(j, m), -2*M0s1(j,
m), 0*M0s1(j, m); ... 0*M0s1(j, m), 0*M0s1(j, m), 1*M0s1(j, m)];

M0pt=[1*M0pt1(j, m), 0*M0pt1(j, m), 0*M0pt1(j, m); ... 0*M0pt1(j, m), -
2*M0pt1(j, m), 0*M0pt1(j, m); ... 0*M0pt1(j, m), 0*M0pt1(j, m), 1*M0pt1(j, m)];

M0st=[1*M0st1(j, m), 0*M0st1(j, m), 0*M0st1(j, m); ... 0*M0st1(j, m), -2*M0st1(j,
m), 0*M0st1(j, m); ... 0*M0st1(j, m), 0*M0st1(j, m), 1*M0st1(j, m)];

M0ptt=[1*M0ptt1(j, m), 0*M0ptt1(j, m), 0*M0ptt1(j, m); ... 0*M0ptt1(j, m),
-2*M0ptt1(j, m), 0*M0ptt1(j, m); ... 0*M0ptt1(j, m), 0*M0ptt1(j, m), 1*M0ptt1(j,
m)];

M0stt=[1*M0stt1(j, m), 0*M0stt1(j, m), 0*M0stt1(j, m); ... 0*M0stt1(j, m), -
2*M0stt1(j, m), 0*M0stt1(j, m); ... 0*M0stt1(j, m), 0*M0stt1(j, m), 1*M0stt1(j,
m)];

NM0=[1*NM01(j, m), 0*NM01(j, m), 0*NM01(j, m); ... 0*NM01(j, m), -2*NM01(j,
m), 0*NM01(j, m); ... 0*NM01(j, m), 0*NM01(j, m), 1*NM01(j, m)];

NM0t=[1*NM0t1(j, m), 0*NM0t1(j, m), 0*NM0t1(j, m); ... 0*NM0t1(j, m), -
2*NM0t1(j, m) , 0*NM0t1(j, m); ... 0*NM0t1(j, m), 0*NM0t1(j, m), 1*NM0t1(j,
m)];

%-----
%----- data 2: normal fault

% 45 degree dip slip fault

% moment tensor: 0, 0, 0; 0, -1, 0; 0, 0, 1;

M0p=[0*M0p1(j, m), 0*M0p1(j, m), 0*M0p1(j, m); ... 0*M0p1(j, m), -1*M0p1(j,
m), 0*M0p1(j, m); ... 0*M0p1(j, m), 0*M0p1(j, m), 1*M0p1(j, m)];

```

M0s=[0*M0s1(j, m), 0*M0s1(j, m), 0*M0s1(j, m); ... 0*M0s1(j, m), -1*M0s1(j, m), 0*M0s1(j, m); ... 0*M0s1(j, m), 0*M0s1(j, m), 1*M0s1(j, m)];

M0pt=[0*M0pt1(j, m), 0*M0pt1(j, m), 0*M0pt1(j, m); ... 0*M0pt1(j, m), -1*M0pt1(j, m), 0*M0pt1(j, m); ... 0*M0pt1(j, m), 0*M0pt1(j, m), 1*M0pt1(j, m)];

M0st=[0*M0st1(j, m), 0*M0st1(j, m), 0*M0st1(j, m); ... 0*M0st1(j, m), -1*M0st1(j, m), 0*M0st1(j, m); ... 0*M0st1(j, m), 0*M0st1(j, m), 1*M0st1(j, m)];

M0ptt=[0*M0ptt1(j, m), 0*M0ptt1(j, m), 0*M0ptt1(j, m); ... 0*M0ptt1(j, m), -1*M0ptt1(j, m), 0*M0ptt1(j, m); ... 0*M0ptt1(j, m), 0*M0ptt1(j, m), 1*M0ptt1(j, m)];

M0stt=[0*M0stt1(j, m), 0*M0stt1(j, m), 0*M0stt1(j, m); ... 0*M0stt1(j, m), -1*M0stt1(j, m), 0*M0stt1(j, m); ... 0*M0stt1(j, m), 0*M0stt1(j, m), 1*M0stt1(j, m)];

NM0=[0*NM01(j, m), 0*NM01(j, m), 0*NM01(j, m); ... 0*NM01(j, m), -1*NM01(j, m), 0*NM01(j, m); ... 0*NM01(j, m), 0*NM01(j, m), 1*NM01(j, m)];

NM0t=[0*NM0t1(j, m), 0*NM0t1(j, m), 0*NM0t1(j, m); ... 0*NM0t1(j, m), -1*NM0t1(j, m), 0*NM0t1(j, m); ... 0*NM0t1(j, m), 0*NM0t1(j, m), 1*NM0t1(j, m)];

%-----

%----- - normal fault

% moment tensor: 1, 0, 0; 0, -1, 0; 0, 0, 0;

M0p=[1*M0p1(j, m), 0*M0p1(j, m), 0*M0p1(j, m); ... 0*M0p1(j, m), -1*M0p1(j, m), 0*M0p1(j, m); ... 0*M0p1(j, m), 0*M0p1(j, m), 0*M0p1(j, m)];

M0s=[1*M0s1(j, m), 0*M0s1(j, m), 0*M0s1(j, m); ... 0*M0s1(j, m), -1*M0s1(j, m), 0*M0s1(j, m); ... 0*M0s1(j, m), 0*M0s1(j, m), 0*M0s1(j, m)];

M0pt=[1*M0pt1(j, m), 0*M0pt1(j, m), 0*M0pt1(j, m); ... 0*M0pt1(j, m), -1*M0pt1(j, m), 0*M0pt1(j, m); ... 0*M0pt1(j, m), 0*M0pt1(j, m), 0*M0pt1(j, m)];

M0st=[1*M0st1(j, m), 0*M0st1(j, m), 0*M0st1(j, m); ... 0*M0st1(j, m), -1*M0st1(j, m), 0*M0st1(j, m); ... 0*M0st1(j, m), 0*M0st1(j, m), 0*M0st1(j, m)];

M0ptt=[1*M0ptt1(j, m), 0*M0ptt1(j, m), 0*M0ptt1(j, m); ... 0*M0ptt1(j, m), -1*M0ptt1(j, m), 0*M0ptt1(j, m); ... 0*M0ptt1(j, m), 0*M0ptt1(j, m), 0*M0ptt1(j, m)];

M0stt=[1*M0stt1(j, m), 0*M0stt1(j, m), 0*M0stt1(j, m); ... 0*M0stt1(j, m), -1*M0stt1(j, m), 0*M0stt1(j, m); ... 0*M0stt1(j, m), 0*M0stt1(j, m), 0*M0stt1(j, m)];

NM0=[1*NM01(j, m), 0*NM01(j, m), 0*NM01(j, m); ... 0*NM01(j, m), -1*NM01(j, m), 0*NM01(j, m); ... 0*NM01(j, m), 0*NM01(j, m), 0*NM01(j, m)];

NM0t=[1*NM0t1(j, m), 0*NM0t1(j, m), 0*NM0t1(j, m); ... 0*NM0t1(j, m), -1*NM0t1(j, m), 0*NM0t1(j, m); ... 0*NM0t1(j, m), 0*NM0t1(j, m), 0*NM0t1(j, m)];

%-----

% calculate the displacement and velocity

reciu(m, :, j) = Const1(m)*Aip(m, :)*M0p+Const2(m)*Ais(m,:)*M0s
+Const3(m)*Afp(m,:)*M0pt+Const4(m)*Afs(m,:)*M0st
+Const5(m)*An(m,:)*NM0;

reciui(m, :, j) = Const1(m)*Aip(m, :)*M0p +Const2(m)*Ais(m,:)*M0s;

reciuf(m, :, j) = Const3(m)*Afp(m,:)*M0pt+Const4(m)*Afs(m,:)*M0st;

reciun(m, :, j) = Const5(m)*An(m,:)*NM0;

reciv(m, :, j) = Const1(m)*Aip(m, :)*M0pt+Const2(m)*Ais(m,:)*M0st
+Const3(m)*Afp(m,:)*M0ptt+Const4(m)*Afs(m,:)*M0stt
+Const5(m)*An(m,:)*(NM0t);

recivi(m, :, j) = Const1(m)*Aip(m, :)*M0pt +Const2(m)*Ais(m,:)*M0st;

recivf(m, :, j) = Const3(m)*Afp(m,:)*M0ptt + Const4(m)*Afs(m,:)*M0stt;

```

recivn(m, :, j) = Const5(m)*An(m,:)*(NM0t);
end
end

% -----

% Save seismogram in each receiver

% One station, one file to record the seismogram: t, x, y, z

% Save the seismograms in .dat files e.g. ONEunc.dat

reco=zeros( Ndt1, 4);
reco1=zeros( Ndt1, 4);
reco2=zeros( Ndt1, 4);
reco3 =zeros( Ndt1, 4);
reco4 =zeros( Ndt1, 4);
reco5 =zeros( Ndt1, 4);
reco6 =zeros( Ndt1, 4);
reco7 =zeros( Ndt1, 4);
reco8 =zeros( Ndt1, 4);
reco9 =zeros( Ndt1, 4);
reco10 =zeros( Ndt1, 4);
reco11 =zeros( Ndt1, 4);
reco12 =zeros( Ndt1, 4);
reco13 =zeros( Ndt1, 4);
reco14 =zeros( Ndt1, 4);
reco15 =zeros( Ndt1, 4);
reco16 =zeros( Ndt1, 4);
reco17 =zeros( Ndt1, 4);
reco18 =zeros( Ndt1, 4);

```

```

reco19=zeros( Ndt1, 4);

for ij=1:Ndt1
reco(ij,1)=t(ij,1);
reco(ij,2)=recivf(1,1,ij)*10e19;
reco(ij,3)=recivf(1,2,ij)*10e19;
reco(ij,4)=recivf(1,3,ij)*10e19;
end

fid = fopen ('ONEunc.dat','w');
save ONEunc.dat reco -ascii
fid = fclose ('all');

for ij=1:Ndt1
reco1(ij,1)=t(ij,1);
reco1(ij,2)=recivf(2,1,ij)*10e19;
reco1(ij,3)=recivf(2,2,ij)*10e19;
reco1(ij,4)=recivf(2,3,ij)*10e19;
end

fid = fopen ('TWOunc.dat','w');
save TWOunc.dat reco1 -ascii
fid = fclose ('all');

for ij=1:Ndt1
reco2(ij,1)=t(ij,1);
reco2(ij,2)=recivf(3,1,ij)*10e19;
reco2(ij,3)=recivf(3,2,ij)*10e19;
reco2(ij,4)=recivf(3,3,ij)*10e19;
end

fid = fopen ('THRununc.dat','w');

```

```

save THRunc.dat reco2 -ascii

fid = fclose ('all');

for ij=1:Ndt1

reco3(ij,1)=t(ij,1);

reco3(ij,2)=recivf(4,1,ij)*10e19;

reco3(ij,3)=recivf(4,2,ij)*10e19;

reco3(ij,4)=recivf(4,3,ij)*10e19;

end

fid = fopen ('FOUunc.dat','w');

save FOUunc.dat reco3 -ascii

fid = fclose ('all');

for ij=1:Ndt1

reco4(ij,1)=t(ij,1);

reco4(ij,2)=recivf(5,1,ij)*10e19;

reco4(ij,3)=recivf(5,2,ij)*10e19;

reco4(ij,4)=recivf(5,3,ij)*10e19;

end

fid = fopen ('FIVunc.dat','w');

save FIVunc.dat reco4 -ascii

fid = fclose ('all');

for ij=1:Ndt1

reco5(ij,1)=t(ij,1);

reco5(ij,2)=recivf(6,1,ij)*10e19;

reco5(ij,3)=recivf(6,2,ij)*10e19;

reco5(ij,4)=recivf(6,3,ij)*10e19;

end

```

```

fid = fopen ('SIXunc.dat','w');
save SIXunc.dat reco5 -ascii
fid = fclose ('all');
for ij=1:Ndt1
reco6(ij,1)=t(ij,1);
reco6(ij,2)=recivf(7,1,ij)*10e19;
reco6(ij,3)=recivf(7,2,ij)*10e19;
reco6(ij,4)=recivf(7,3,ij)*10e19;
end
fid = fopen ('SEVunc.dat','w');
save SEVunc.dat reco6 -ascii
fid = fclose ('all');
for ij=1:Ndt1
reco7(ij,1)=t(ij,1);
reco7(ij,2)=recivf(8,1,ij)*10e19;
reco7(ij,3)=recivf(8,2,ij)*10e19;
reco7(ij,4)=recivf(8,3,ij)*10e19;
end
fid = fopen ('EIGunc.dat','w');
save EIGunc.dat reco7 -ascii
fid = fclose ('all');
for ij=1:Ndt1
reco8(ij,1)=t(ij,1);
reco8(ij,2)=recivf(9,1,ij)*10e19;
reco8(ij,3)=recivf(9,2,ij)*10e19;
reco8(ij,4)=recivf(9,3,ij)*10e19;

```

```

end

fid = fopen ('NINunc.dat','w');
save NINunc.dat reco8 -ascii

fid = fclose ('all');

for ij=1:Ndt1

reco9(ij,1)=t(ij,1);

reco9(ij,2)=recivf(10,1,ij)*10e19;
reco9(ij,3)=recivf(10,2,ij)*10e19;
reco9(ij,4)=recivf(10,3,ij)*10e19;

end

fid = fopen ('MIDunc.dat','w');
save MIDunc.dat reco9 -ascii

fid = fclose ('all');

for ij=1:Ndt1

reco10(ij,1)=t(ij,1);

reco10(ij,2)=recivf(11,1,ij)*10e19;
reco10(ij,3)=recivf(11,2,ij)*10e19;
reco10(ij,4)=recivf(11,3,ij)*10e19;

end

fid = fopen ('SYIunc.dat','w');
save SYIunc.dat reco10 -ascii

fid = fclose ('all');

for ij=1:Ndt1

reco11(ij,1)=t(ij,1);

reco11(ij,2)=recivf(12,1,ij)*10e19;
reco11(ij,3)=recivf(12,2,ij)*10e19;

```



```

reco11(ij,4)=recivf(12,3,ij)*10e19;
end
fid = fopen ('SERunc.dat','w');
save SERunc.dat reco11 -ascii
fid = fclose ('all');
for ij=1:Ndt1
reco12(ij,1)=t(ij,1);
reco12(ij,2)=recivf(13,1,ij)*10e19;
reco12(ij,3)=recivf(13,2,ij)*10e19;
reco12(ij,4)=recivf(13,3,ij)*10e19;
end
fid = fopen ('SSAunc.dat','w');
save SSAunc.dat reco12 -ascii
fid = fclose ('all');
for ij=1:Ndt1
reco13(ij,1)=t(ij,1);
reco13(ij,2)=recivf(14,1,ij)*10e19;
reco13(ij,3)=recivf(14,2,ij)*10e19;
reco13(ij,4)=recivf(14,3,ij)*10e19;
end
fid = fopen ('SSIunc.dat','w');
save SSIunc.dat reco13 -ascii
fid = fclose ('all');
for ij=1:Ndt1
reco14(ij,1)=t(ij,1);
reco14(ij,2)=recivf(15,1,ij)*10e19;

```

```

reco14(ij,3)=recivf(15,2,ij)*10e19;
reco14(ij,4)=recivf(15,3,ij)*10e19;
end

fid = fopen ('SWUunc.dat','w');
save SWUunc.dat reco14 -ascii

fid = fclose ('all');

for ij=1:Ndt1
reco15(ij,1)=t(ij,1);
reco15(ij,2)=recivf(16,1,ij)*10e19;
reco15(ij,3)=recivf(16,2,ij)*10e19;
reco15(ij,4)=recivf(16,3,ij)*10e19;
end

fid = fopen ('SLIunc.dat','w');
save SLIunc.dat reco15 -ascii

fid = fclose ('all');

plotseismogram(reciu, reciv, reciuf, recivf, reciui, recivi, reciun, recivn,gnum,t);
%plot seismogram fprintf(' - Time at the end %.2f ', toc)

return

```

Appendix B: Moment Tensor Retrieval - A MATLAB GUI

ISOLA and ISOLA-GUI are two parts of ISOLA moment tensor retrieval software package. They are free package made by Zahradnik and Sokos (2008) and can be downloaded via Internet.

The method is applicable for regional and local events. Instrumentally corrected band-pass filtered velocity records are used. The code transforms velocity into displacement, inverts the displacement, and also provides synthetic displacement.

ISOLA only considers far-field terms to do moment tensor inversion. To consider intermediate-field terms into ISOLA, I use the following equations from B.7 to B.12. Aki and Richards point out in their book (2002) that the displacements caused by a double couple are calculated as:

$$\begin{aligned}
 u(\vec{x}, t) = & \frac{1}{4\pi\rho} \vec{A}^N \frac{1}{r^4} \int_{r/\alpha}^{r/\beta} \tau M_0(t - \tau) d\tau \\
 & + \frac{1}{4\pi\rho\alpha^2} \vec{A}^{IP} \frac{1}{r^2} M_0(t - \frac{r}{\alpha}) + \frac{1}{4\pi\rho\beta^2} \vec{A}^{IS} \frac{1}{r^2} M_0(t - \frac{r}{\beta}) \\
 & + \frac{1}{4\pi\rho\alpha^3} \vec{A}^{FP} \frac{1}{r} \dot{M}_0(t - \frac{r}{\alpha}) + \frac{1}{4\pi\rho\beta^3} \vec{A}^{FS} \frac{1}{r} \dot{M}_0(t - \frac{r}{\beta})
 \end{aligned} \tag{B.1}$$

\vec{A}^N represents near-field radiation pattern:

$$\vec{A}^N = 9\sin 2\theta \cos \phi \hat{r} - 6(\cos 2\theta \cos \phi \hat{\theta} - \cos \theta \sin \phi \hat{\phi}) \tag{B.2}$$

\vec{A}^{IP} and \vec{A}^{IS} represent intermediate-field radiation pattern:

$$\vec{A}^{IP} = 4\sin 2\theta \cos \phi \hat{r} - 2(\cos 2\theta \cos \phi \hat{\theta} - \cos \theta \sin \phi \hat{\phi}) \tag{B.3}$$

$$\vec{A}^{IS} = -3\sin 2\theta \cos \phi \hat{r} + 3(\cos 2\theta \cos \phi \hat{\theta} - \cos \theta \sin \phi \hat{\phi}) \tag{B.4}$$

\vec{A}^{FP} and \vec{A}^{FS} represent far-field radiation pattern:

$$\vec{A}^{FP} = \sin 2\theta \cos \phi \hat{r} \quad (\text{B.5})$$

$$\vec{A}^{FS} = \cos 2\theta \cos \phi \hat{\theta} - \cos \theta \sin \phi \hat{\phi} \quad (\text{B.6})$$

Their principal findings are that far-field displacements still attenuate as r^{-1} and are proportional to particle velocity at the source. Some certain remarkable similarities are found between far-field, intermediate-field, and near-field radiation patterns. The final displacement eventually reaches a final fixed offset, attenuates as r^{-2} .

From Equation B.1, we can also find out that the far-field terms attenuate as r^{-1} , and the intermediate-field terms attenuate as r^{-2} . The coefficient different in the far-field terms and intermediate-field terms is the velocity. Compared with Equation B.3, B.4, B.5, and B.6, I get the following equation:

$$\vec{A}^{IP} = 4\vec{A}^{FP} - 2\vec{A}^{FS} \quad (\text{B.7})$$

$$\vec{A}^{IS} = -3\vec{A}^{FP} + 3\vec{A}^{FS} \quad (\text{B.8})$$

Let us define some parameters:

$$\frac{1}{4\pi\rho\alpha^3}\vec{A}^{FP}\frac{1}{r} = X_p \quad (\text{B.9})$$

$$\frac{1}{4\pi\rho\beta^3}\vec{A}^{FS}\frac{1}{r} = X_s \quad (\text{B.10})$$

$$\frac{1}{4\pi\rho\alpha^2}\vec{A}^{IP}\frac{1}{r^2} = X_{pp} \quad (\text{B.11})$$

$$\frac{1}{4\pi\rho\beta^2}\vec{A}^{IS}\frac{1}{r^2} = X_{ss} \quad (\text{B.12})$$

X_p and X_s are the major part of far-field terms of displacement caused by P-wave and S-wave. Meanwhile, X_{pp} and X_{ss} are the major part of intermediate-field terms of displacement caused by P-wave and S-wave.

Then Equation B.7 and B.8 are used into B.11 and B.12, the relationship between the major part of far-field terms of displacement caused by P-wave and S-wave and intermediate-field terms is shown below:

$$X_{pp} = X_p \alpha / r \quad (\text{B.13})$$

$$X_{ss} = X_s \beta / r \quad (\text{B.14})$$

The displacement with far-field terms and intermediate-field terms is shown in Equation B.15.

$$\begin{aligned} u(\vec{x}, t) &= \frac{1}{4\pi\rho\alpha^2} \vec{A}^{IP} \frac{1}{r^2} M_0(t - \frac{r}{\alpha}) + \frac{1}{4\pi\rho\beta^2} \vec{A}^{IS} \frac{1}{r^2} M_0(t - \frac{r}{\beta}) \\ &\quad + \frac{1}{4\pi\rho\alpha^3} \vec{A}^{FP} \frac{1}{r} \dot{M}_0(t - \frac{r}{\alpha}) + \frac{1}{4\pi\rho\beta^3} \vec{A}^{FS} \frac{1}{r} \dot{M}_0(t - \frac{r}{\beta}) \quad (\text{B.15}) \\ &= X_{pp} M_0(t - \frac{r}{\alpha}) + X_{ss} M_0(t - \frac{r}{\beta}) + X_p \dot{M}_0(t - \frac{r}{\alpha}) + X_s \dot{M}_0(t - \frac{r}{\beta}) \end{aligned}$$

The final V_p and V_s is the velocity contains both far-field terms and intermediate-field terms. These are the equations I derive from Aki and Richards (2002).

Based on the equations (Equation B.7 to Equation B.14), I modify the fortran code GRXYZ.FOR in ISOLA as follows:

line 1679 to 1683:

```
cdu7=(k5(jrs)*cu3 - cs6*k2(jrs)*s6)*1+(vp/rr(ir))*(4*k5(jrs)*cu3 -
2*cs6*k2(jrs)*s6)
cdu8=(k2(jrs)*cu3 - cs6*k5(jrs)*s6)*1+(vp/rr(ir))*(3*k2(jrs)*cu3 -
3*cs6*k5(jrs)*s6)
```

The environment to run ISOLA is MATLAB R2010b (7.11.0), and R2011a as well. The system is 32-bit operate system. ISOLA can works in 64-bit operate

system, but one need to change at least three sentences in MATLAB code. The fortran code of ISOLA can be compiled in 32-bit operate system using Microsoft Fortran Compiler or PowerStation. The version I used to compile fortran code is Compaq Fortran 7.0 which can be installed in 32-bit Windows XP or previous system. GCC and Gfortran cannot compile the fortran code correctly.

ISOLA can only output the double couple of moment tensor correctly. If you want to output the beach-ball of CLVD, one can use GMT, the sentences are as follows:

```
pscoast -R19.40000/19.60000/19.40000/19.60000 -JM10 -G255/255/204 -Df -
W0.7p -P -B0.1 -K -S104/204/255 -Lf19.50/19.50/19.50/10 > sources.ps
```

```
psxy -R -JM10 sources.gmt -Sd0.2 -M -W1p/0 -K -O -G255/0/0 >> sources.ps
```

```
pstext -R -JM10 sources.txt -N -O -K -D0.2/0 >> sources.ps
```

```
psmeca -R -JM10 -Sm1.5i beachb.foc -V -O -C1 -N >> sources.ps
```

They can output the beach-ball of CLVD in a correct way as well as isotropic part of any moment tensor.

Appendix C: Steps for Inversion by ISOLA

To run ISOLA properly, one should follow the following steps.

TABLE C.1: The Inversion Steps

Step	Function
Define Crustal Model	Input the velocity of the formation Depth (km), Vp (km/s), Vs (km/s), Density type 999 in depth as an end signal.
Event Info	Input the source information The latitude and longitude of the source Choose a proper duration time or change the duration in the duration.isl the number is = time interval * 8191
Station Selection	Choose the stations or receivers Set up a .stn file The name of a station should be 3 capital letters follow a tab, and input latitude, a tab, and longitude eg. ONE 10.00 10.00
	Load all the synthetic seismograms Create corresponding filter first In the pzfiles directory The name of filter is consist with station name Use the number of zeros and poles for filter
Continued on next page	

Table C.1 – continued from previous page

Step	Function
Data Preparation	<p>Pick up number refer Poles, Zeros, and Filter</p> <p>Three .pz files (3 directions) are needed</p> <p>Load Ascii file, choose the seismogram</p> <p>Click Inst. Correction to filter the seismogram</p> <p>Plot Response to show how the filter works</p> <p>Origin Allign for the seismograms not from time 0</p> <p>Save data (raw data)</p>
Seismic Source Definition	<p>Choose the depth to calculate</p> <p>Click Source below epicenter</p> <p>Starting depth must be larger than 5</p> <p>Depth step is default 1</p> <p>No of Sources is 1 or more</p>
Green Function	<p>Calculate the Green Function for the source</p> <p>Call GRXYZ.for and elemse.for code</p> <p>Calculate the green function</p> <p>Rename the one including</p> <p>the intermediate-field terms</p>
Inversion	<p>Calculate the strike, dip, and rake angle for the source</p> <p>Full MT</p> <p>ISO, CLVD, and DC</p> <p>Deviatoric MT</p> <p>DC and CLVD</p>
Continued on next page	

Table C.1 – continued from previous page

Step	Function
	DC constrained Only DC part for inversion
Plot Result	Plot the 'beach ball' based on the inversion results Plot moment tensor Call GMT to plot the inversion result in 'beach ball' Change the GMT code as in Appendix B for plot CLVD

Vita

Chennu Fan was born in 1988, in Changping, Beijing, China. She finished her undergraduate studies in geophysics from University of Science and Technology of China in July 2010. In August 2011, she came to Louisiana State University (LSU) to pursue graduate studies in Petroleum Engineering under the supervision of Dr. Arash Dahi Taleghani for master's degree. She will receive her Master of Science in Petroleum Engineering degree in May, 2014.